Spring 2011

Growth of Alkali Antimonide Photosensitive Thin Films

George Annobil
Old Dominion University

GROWTH OF ALKALI ANTIMONIDE PHOTOSENSITIVE THIN FILMS

by

George Annobil
B.S. May 2009, Old Dominion University

A Thesis Submitted to the Faculty of
Old Dominion University in Partial Fulfillment of the
Requirements for the Degree of

MASTER OF SCIENCE

ELECTRICAL ENGINEERING

OLD DOMINION UNIVERSITY
May 2011

Approved by:

_____

Ravindra P. Joshi (Director)

_____

Matt Poelker (Member)

_____

Helmut Baumgart (Member)

GROWTH OF ALKALI ANTIMONIDE PHOTOSENSITIVE THIN FILMS

ABSTRACT

George Annobil
Old Dominion University, 2011
Director: R. P. Joshi

The experiment performed in this research addresses the growth of an alkali antimonide photosensitive film. Research was conducted to understand and develop a growth technique for a unique vapor deposition system in a vacuum environment. Specifically, the grown film will be utilized as a photocathode, and hence quantum efficiency (QE) and photocathode lifetime measurements are conducted. The research presents the successful growth of the binary compound cesium antimonide with achieved quantum efficiency of ~0.07% at ~240V anode bias. This experimental result demonstrated that the deposition technique was reliable in producing a feasible cathode. It further allowed the verification of theoretical alkali antimonide properties. Future work will be to adopt the technique to produce the ternary alkali antimonides, such as cesium potassium antimonide.

Gallium Arsenide (GaAs) is currently the primary semiconducting photocathode used for operation in many Free Electron Laser (FEL) particle accelerators such as at the one at Jefferson Laboratory, Newport News, Virginia. However, several alkali antimonides are being pursued as prospective substitutes. These are generally expected to have several properties that make them better alternatives for synchrotron accelerators. These properties include greater lifetimes, greater QE and vacuum quality tolerance compared to GaAs. Therefore, the thesis research measures the QE, lifetime of the alkali antimonide to attempt to verify these attributes. The crystal growth experiments were carried out in the Source Lab of Jefferson Laboratory.

This thesis is dedicated to my parents who have shown unconditional love and support throughout my studies. It is also dedicated to all my friends and relatives who have likewise encouraged me and believed that I could achieve my goals.

ACKNOWLEDGMENTS

I would like to thank my Advisor, Dr Ravindra Joshi, for his guidance over the years regarding my undergraduate and post graduate work. I would also like to thank the following people for their assistance in their respective ways. My thanks to Matt Poelker, my assigned supervisor at Jefferson Laboratory, for proposing and acquiring funding for this project. My thanks also to Marcy Stutzmun and Phil Adderely, physicist and lead vacuum technician, for their advice and technical guidance regarding accelerator and vacuum physics. Finally, I would also like to thank John Smedley and Andrew Burrill for their communication and support concerning cesium potassium antimonide thin films and general film growth techniques. The research project was funded and carried out on location at Jefferson National Laboratory in Newport News.

TABLE OF CONTENTS

LIST OF TABLES

Table Page

LIST OF FIGURES

Figure Page

CHAPTER I

INTRODUCTION

1.1 Introduction

Chapter One of this thesis provides as an overview of the main goals of the thesis work and a brief description of the scientific fields where the work has relevance. Furthermore, the chapter explains elementary concepts involved in the research work and the impact that its success would have in the science and engineering fields. Section 1.2 discusses electron beams in general; it describes electron beams and some of their modern day applications. Furthermore 1.2 discusses some technologies incorporating electron beams. This section also describes the various recent sources used to produce electron beams, the physical properties that permit the emission phenomenon, and external means by which the beams are manipulated to have a desired direction and beam emittance. With respect to recent beam producing technologies, two main types are addressed; DC photoguns and RF photoinjectors. Section 1.3 covers the scope of the project; explaining the extent of work that is carried out in the research, the data obtained and the future prospects of the work. Therefore, it provides a more detailed explanation of the work undertaken and addresses the expectations of the project, including the data that must be collected. A discussion of the location of this work and other facilities that have previously been involved and/or are carrying out similar work is also given. The chapter also includes a discussion of technological

research applications of the fabricated film at Jefferson Laboratory, and finishes with description of future work that will be continued at the laboratory.

1.2 Electron Beams Sources

Electron beams, also referred to as cathode rays, are a stream of electrons or electron bunches that are generally produced from a cathode electrode and accelerated under an electric field to an anode electrode, and occur in the presence of a vacuum environment. Electron beams were first observed by the German physicist Johann Hittorf in 1869. Then in 1876 Eugene Goldstein named the stream of particles, which were not yet fully understood at the time, as cathode rays. In 1897, British physicist J. J. Thomson demonstrated that rays were actually composed of negatively charged particles that would later be named electrons [1]. One of the earliest and most common known applications of the electron beam is in Cathode Ray Tubes (CRTs) that create the images in conventional television sets.

In recent years the use of electron beams in particle physics has been a critical component for the study of subatomic particles in this field. It is therefore essential to have a reliable, consistent and durable source to produce these beams. One such source is a photocathode, which can be a metallic, liquid or non-metallic semiconducting thin-film that emits electrons through photoemission. The photoemission process is a result of the photoelectric effect, a phenomenon explained by Albert Einstein in the early 20^{th} century – awarding him the Nobel Prize in 1921 [2]. During photoemission, the liquid, solid or gaseous

photocathode absorbs photon energy from electromagnetic radiation, typically within the visible or near-ultraviolet spectrum. In metals, electrons in the valence band must be sufficiently energized from the absorbed photons to overcome the metal's workfunction and elevate to the vacuum level. However, if a photosensitive semiconducting material is used as the electron source, then the electrons need to obtain energy that is close to the material's bandgap energy or greater. In the field of particle physics, an accelerator can be used to produce the electron beams that are used to study nucleons. In nuclear-physics facilities, the energy level of the electron beam allows different degrees of probing that can be done for atomic nucleons. "A beam whose energy ranges from 1MeV to 1 GeV, for instance, can probe how quarks and gluons make up protons and neutrons in an atom's nucleus [2]". Accelerator machines with even higher-energy levels exist at SLAC (National Accelerator Facility), formerly called the Stanford Linear Accelerator Center – located at Stanford University, and Jefferson Lab's Continuous Electron Beam Accelerator Facility is working towards a 12 GeV machine. These energy levels permit the study of deeper nucleon matter such as "constituent quarks and their interplay with the quark sea that makes up a nucleon [2]". Another aspect that is also of interest in particle physics is the polarization of the electron beam that allows researchers to "study the spin structures of nuclei [2]". At the heart of the accelerator is the electron source, which may be a photocathode. The most widely used photocathode for producing electron beams source is Gallium Arsenide (GaAs). Depending on the source, the emitted electrons may either be polarized or non-polarized. GaAs is capable of emitting

polarized electrons when illuminated with light that has a "circular polarization [2]". An electron beam is said to be polarized when the two spin states that exist are unevenly populated [3]. The wavelength of light that must be used to illuminate a GaAs crystal is 860nm which corresponds to its bandgap energy of 1.46eV. "The circularly polarized light excites electrons across the gap from two degenerate valence band-band states – $P_{1/2}$ and $P_{3/2}$ states [2]". This is interpreted to mean that for every one electron that is promoted to one spin state, three are elevated to the other state. This is illustrated in Figure 1, which illustrates the emission of electrons from either state –"the solid and dashed lines represent two different transitions that utilize a particular helicity of polarized light – "either left-handed or right-handed [1]". This form of excitation is known to produce a 50% polarization in GaAs. In practice, this polarization value is limited to approximately 35% due to "depolarization effects such as lattice imperfections and inelastic scattering of electrons that occurs during diffusion and emission [2]".

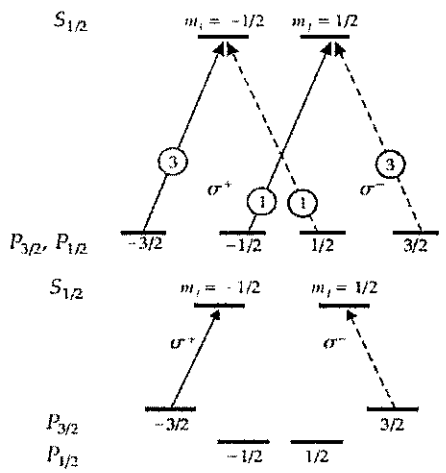

Figure 1: Polarized Electron Emission in GaAs [2].

However, other accelerator facilities have an alternative use for electron beams, namely as light sources. A light source is the terminology used to describe the specific technology that is used for the study of molecular particles in physics and organic materials in the field of biology. What makes light sources unique is the type of radiation they emit during their operation. The radiation is given off when the electrons are interact with a magnetic field while moving at velocities close to that of light – the radiation wavelength typically creates high-peak-power x-rays or high-average-power infrared [2], giving out high-intensity, monochromatic radiation. Light source technology has been developed over the years starting from first-generation progressing to fourth-generation light sources, with the difference being the type of accelerator technology that is utilized [2]. Physicists at Jefferson Lab in Newport News, utilize a fourth-generation light source in the form of a free electron laser (FEL) in their research. The electron source in this case, and traditionally, has been the GaAs photocathode. However, there are also several semiconductor photocathodes under investigation for use as electron beam light sources. These semiconductor photocathodes are often in the form of alkali metal antimonides. Some notable research facilities that have done work in this area include Brookhaven National Laboratory in New York, the Stanford Synchrotron Radiation Lightsource (SSRL) is a synchrotron light user facility located on the SLAC campus, researchers from the Boeing Defense and Space Group and Computer Services, and the Bhabha Atomic Research Center in Bombay, India. There has been previous work conducted in the past that suggests several advantages to using these alkali semiconducting films as opposed to

GaAs. Primarily these advantages include, a higher tolerance to lower quality vacuum environments, their prompt emitting properties – quick response both to the onset of illumination and the removal of incident illumination. Furthermore, they have the capability of producing higher average currents as well higher cathode lifetimes in an accelerator.

1.3 Scope of Thesis Research

The research undertaken for this thesis was in the area of semiconductor technology aimed at producing a specialized photosensitive thin film. The work involved gaining an understanding of the theoretical process to successfully grow binary and ternary compound alkali antimonides; namely cesium antimonide (Cs3Sb) and cesium potassium antimonide (K_2CsSb), respectively. Towards this end, a literature review was carried out to understand the stoichiometry of the proposed cathode and the reasoning behind the chosen elements that compose the thin film. There have been a number of methodologies that have been applied in the growth of alkali antimonide cathodes, and this thesis describes some of these methods. Traditionally, however these cathodes have been grown using a vacuum deposition system – utilizing physical vapor deposition (PVD) of the element sources. This was the approach utilized in the research. The cesium, antimony and potassium elements were vaporized from thermal sources and chemically reacted to form a crystalline thin film on a chosen substrate material placed above the sources. Therefore, after installing these sources in a vacuum chamber, the research required characterization of these sources within the unique dimensions of the chamber. The second phase of the research was to successfully grow a

cathode and characterize its behavior. The characterization of the cathode allowed conclusions and comparisons to be drawn in regard to how the cathode could function and a substitute to GaAs in a light source. Therefore data was collected that demonstrates the capabilities of the cathode. A property of particular interest is the quantum efficiency (QE) of the photocathode. Quantum efficiency can be described as the ratio of photons that are incident on a photocathode and utilized in the absorption process to elevate electrons, versus all photons incident on the photocathode. The quantum efficiency differs as a function of the electromagnetic wavelength applied to the cathode; therefore, the research included the study of this wavelength variable. Furthermore, the research work involved the optimization of this quantum efficiency value for the grown cathode. Some of the primary methods proposed to do this includes finding a suitable substrate and experimentally finding the appropriate thickness ratios of the deposited material that produces the greatest photocurrent. The lifetime of the cathode is also a quantity of interest, which measures the time span that must be elapsed to completely deteriorate the QE of a cathode to zero. Another quantity of interest is the polarization of the beam produced by the cathode. Although polarization is not of concern for the purposes of a FEL, knowing the polarization characteristics may be useful for ulterior high-energy physics experiments. Although no polarization is required for the functioning of a light source, a moderate quantity (or higher), however is required to allow greater capabilities for nuclear physics studies. The future of the thesis research lies in the application of the cesium potassium antimonide cathode in a field electron laser. In a FEL, an electron beam

produced is manipulated by a "wiggler" – a series of alternating-polarity magnetic fields that effectively cause the electrons to vibrate at a frequency that results in the emission of monochromatically tuned light. This endeavor was attempted using Jefferson Lab's FEL housed at the Continuous Electron Beam Accelerator facility (CEBAF). The image of the wiggler at Jefferson Lab is displayed in Figure 2. Despite the expected advantages of the cesium potassium antimonide film in an electron gun, there has not been a standardized comparison between the output from GaAs and that of K_2CsSb. Future research could include a broader range of experiments that can be conducted regarding the study of quarks. The thesis research documents and describes a reproducible method that has successfully made the first alkali antimonide photocathode grown at Jefferson Laboratory.

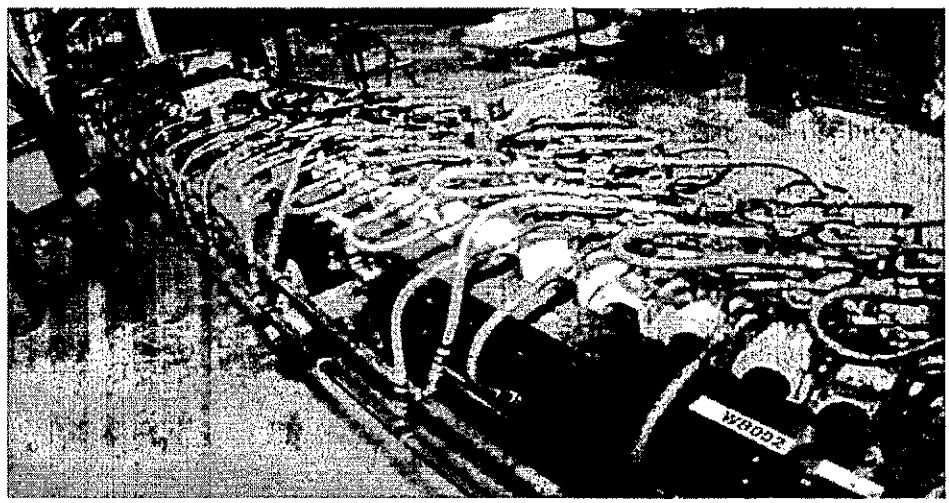

Figure 2: The wiggler at Jefferson Laboratory, Newport News [2].

CHAPTER II

THEORY AND BACKGROUND

2.1 Introduction

This chapter provides discussions of the theories that are employed toward the growth of alkali antimonide cathodes. A typical example of such a material is cesium potassium antimonide. This chapter also describes the concept behind the photoelectric effect that produces photoemission in these photosensitive cathodes. The theory for the generation of polarized electrons from GaAs is also described in order to understand similarities and differences between the two types of thin films. Section 2.2 introduces the main ideas regarding the utilization of physical vapor deposition (PVD) for the growth of thin films. Then in section 2.2.1, the methodology is applied to characterize the output for the sources chosen for the various experiments. The remainder of the chapter goes on to describe the reasoning behind the choice of materials. It includes a discussion of photoemission from alkali metal antimonides in general, and the differences between these materials and GaAs.

2.2 Physical Vapor Deposition (PVD) and Vacuum Theory

Physical vapor deposition (PVD) methods are a prominent physical approach for the growth of thin films. Accordingly, physical vapor deposition processes are also commonly referred to as thin film processes. When using PVD, atoms or molecules are vaporized from a source within vacuum system. These atoms or molecules then collect, possibly react chemically, and condense on a

substrate to form a layer or multiple layers of film. The films produced, as expected for thin films, usually range in thickness from a few nanometers to micrometers [4]. There are some primary methods of PVD, namely vacuum evaporation, sputter deposition, and ion plating. One of the simpler methods out of these four processes is vacuum evaporation where a "thermal" source is the origin of the vaporized material. The thermal sources can take various forms, such as element alloys strips that are heated electrically by running a prescribed current through the strips to alleviate the gas. Other sources consist of more elaborate devices; including "boats" or crucibles that can contain pellets of a required element that can be housed in a wire filament, and hence heated via the filament to raise the pellets to sufficient temperatures for vaporization. One eccentric device known as an E-gun, directs energized electrons emitted thermionically from a filament to the source container to heat the source material [4].

One of the most critical aspects of PVD processes is to obtain a high vacuum environment for the system. This is required to helps prevent the contamination of the film from extraneous gases that may be present within an experiment chamber. Furthermore, high vacuum promotes the increase of the mean free path. The mean free path can be described as the distance that a gas particle can move without colliding with any other particles. Experiments generally require at least high vacuum of about 10^{-6} Torr to be (more) viable. With the presence of residual gases in a chamber, that is the poorer the vacuum, the greater is the length of time required to deposit a desired thickness of film. A Langmuir (L) represents a unit of dosage of an applied gas to a given substrate;

defined by multiplying the gas pressure by the exposure time of the gas. Formally, one Langmuir corresponds to an exposure of 10^{-6} Torr during one second [5]. Furthermore, depending on the sticking coefficient; a property that varies based on the substrate and impinging molecule reactivity, one Langmuir generally results in the deposition of a monolayer of a material. A monolayer describes a single layer of either atoms or molecules of material. Therefore generally speaking, it is desired that the partial pressures of ambient gases in the vacuum be much lower than that of the vapor of the required deposition material.

An essential theory that is involved in physical vapor deposition is the kinetic theory of gases. The kinetic theory of gases is utilized to gain an understanding of the behavior. "It provides estimates of the impingement rate, mean free path, heat capacity, diffusivity, viscosity, and thermal conductivity, parameters that frequently bear on the deposition kinetics and purity of a thin film [6]". Furthermore, it is useful in "predicting the output of physical vapor deposition sources [6]". The theory assumes that the gas particles are infinitely hard spheres, and that an extremely large number of particles undergo elastic collisions with no other forces applied on to them except those that incur during collisions with each other or the container [6].

Under the kinetic theory of gases, a statistical point of view regarding the energies of the gas particles can then be discussed that is based on the Boltzmann distribution function. "The distribution in energy of the particles is given by the classical Boltzmann distribution function, and is appropriate for identical and distinguishable particles that do not obey the Pauli Exclusion Principle [6]":

$$f(E) = exp\frac{-E}{kT} \quad (1)$$

In the above equation T is the absolute temperature, k is the Boltzmann constant, and E is the energy. "The number of particles having energy between E and $E+dE$ is therefore given by Nf(E)dE/kT, where N is the total number of particles and 1/kT is the necessary normalizing factor. The distribution function is also sometimes referred to as the Maxwellian or Maxwell-Boltzmann distribution [6]. Furthermore, the Boltzmann factor which is important for "thermally activated rate processes, [6] "gives the fraction of the total number of particles in the system whose energy is greater than or equal to some specified energy, say E_a. It is calculated from the equation below. The thermally activated processes can exhibit a temperature dependence given by the same equation. The rate can be plotted in the form of an Arrhenius plot; a plot of log(rate) vs. 1/T, and a straight line is obtained. The slope of the line is $-E_a/k$ and E_a is the thermal activation energy [6]". The processes are denoted thermally activated since only particles with energy E_a can be involved in these processes.

$$\int_{E_a}^{\infty} exp\frac{-E}{kT}\frac{dE}{kT} = exp\frac{-E_a}{kT} \quad (2)$$

Such thermal deposition processes occurring in a vacuum belong to a category of PVD processes suitably named "vacuum deposition". "The material vaporized from the source typically has a composition which is in proportion to the relative vapor pressures of the material in the molten source material [4]". To estimate the mass of vaporized material that is emitted in a particular direction from a thermal source, an approximation distribution of the atomic or molecular

particle flux is required. Typically the flux distribution "can be described by a cosine distribution [4]". With ideally very little to no particle collisions, due to the presence a good quality vacuum, the vapor material deposits in a straight, "line-of-sight [4]" manner, from source to substrate. If a point source approximation is made for the source, then the distribution of the molecules or atoms vaporized, and the corresponding mass deposited on the substrate is related by the following equation [4]:

$$\frac{dm}{dA} \propto \frac{cos\Phi cos\theta}{r^2} \tag{3}$$

where dm/dA is mass per unit area deposited on a planar substrate above the source, r is the distance from the source to substrate, θ is the angle normal to the surface of the source and Φ is the angle from the source. This relation of the flux distribution is illustrated in Figure 3. Therefore, to get an approximation of the total mass deposited on the surface of a planar substrate, the integration over the entire surface needs to be calculated. However, it is important to stress that the cosine distribution is only an approximation and may not hold true due to non-ideal source geometry, "collisions associated with high vaporization rates and the level of vaporant in the source [4]".

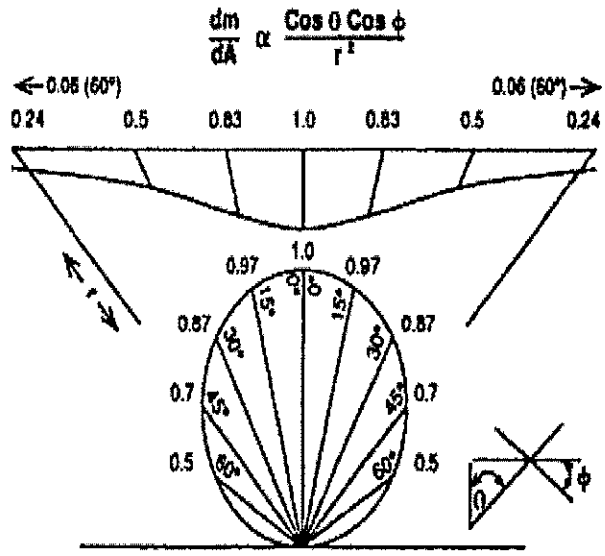

Figure 3: Cosine distribution of vaporized material [4].

Within a vacuum chamber, all materials contribute gaseous pressure known as the equilibrium vapor pressure or partial pressure. At a steady temperature, a gas at equiliubrium pressure vapor pressure has an equal amount of molecules leaving a surface as the number returning to the surface. Vacuum chamber environments generally have contaminant gases that arise from, residual vapors, desorption of water from surfaces or deposition fixtures and substrates, outgassing from source materials and chamber leakage. Between the 10^{-5} and 10^{-7} Torr range, water vapor from outgassing and desorption is the dominant contaminant, whereas under ultra high vacuum (~10^{-9} Torr) hydrogen is more common [4]. To minimize the presence of contaminants on metal fixtures placed within the chamber, metal surfaces typically undergo a cleaning process: an initial detergent wash, followed by a rinsing with de-ionized water, and finally another rinse with acetone.

2.3 Photoelectric Effect and Photoemission Process

The photoelectric effect is commonly known as the phenomenon where electrons are emitted from and out of a given material in the presence of electromagnetic (light) that is incident on the material. These materials may be of several forms such as metals, gases or semiconductors. However, some books use the term "photoelectric effects" to encompass three distinct phenomena involving the interaction of light with matter. Zworykin and Ramberg specifically refer to the emission of electrons from a material due to excitation from electromagnetically radiation as the "photoemissive effect." This is contrasted from two other effects; the photovoltaic and the photoconductive effect [7]. The "photoemissive effect was the last to appear on the scene; yet it has contributed most to our understanding of the interaction of light with matter and has outstripped both the other photoelectric effects in the importance of its applications[7]". "The photoemissive effect was discovered by Hertz in 1887, as a by-product of his classical researches on electric waves and oscillations [7]". The photovoltaic effect is similar to the photoemissive effect except that the electrons do not escape the material, but are excited to higher band energy levels to set establish a potential difference within the material. "Edmond Becquerel appears to have been the first person to observe the action of light in generating an electric current or voltage. In his experiments, carried out as early as 1839, a pair of electrodes was immersed in a liquid electrolyte, or two layers of electrolytes, such as ferric chloride solution and alcohol, capable of reacting with each other. The current generated when the cell was illuminated with sunlight was measured by a

galvanometer connected between the two electrodes [7]". The photoconductive effect refers to the drop in a materials resistance due to the incidence of light on its surface. This effect was discovered by Willoughby Smith in 1873 when he saw a change in the conductivity of selenium when exposed to light [7].

Albert Einstein is credited with having developed an explanation of the photoemissive phenomenon. "In 1905 Albert Einstein proposed that photoemissive phenomena could be accounted for by adopting Planck's quantum theory of radiation and assuming that, when a quantum of energy $h\nu$ reacted with an electron, the latter would acquire the total quantum and be released in possession of an equivalent amount of kinetic energy [7]." His equation for the kinetic energy for the photoelectron is [7]

$$eV = \frac{mv^2}{2} = h\nu - W \tag{4}$$

where W, the workfunction, represents the excess of energy which the electron has to expend to free itself from the body of the emitting substance over the energy it possessed originally, before its reaction with the quantum of energy. W is a constant for any one electron of the substance. The kinetic energy can be expressed in electron volts as eV, where V is the retarding potential required to stop the fastest photoelectrons [7]". Equation (4) expresses and corroborates the first and second empirical laws that state that the energy of emission increases linearly with the exciting radiation, and "the number of electron released are proportional to the intensity of the light [7]", respectively.

The photoemission from metals has unique characteristics to that of semiconductor films and can be explained with the aid of a band structure diagram near the material surfaces. In metals photons are required to excite the electrons above the metal's workfunction, "the difference between the Fermi level E_F and the vacuum energy level $E_{vac,}$ where the electron is free [2]". This is illustrated in Figure 3a. However when dealing with semiconductors, electrons have to overcome the bandgaps of the material. The material can have either positive electron affinity (P.E.A.) or negative electron affinity (N.E.A.). Electron affinity generally refers to the energy that separates the bottom of the conduction band to the vacuum level. For negative electron affinity materials, the vacuum energy level is below the bottom of the conduction band, as in Figure 3b, and in positive electron affinity materials the vacuum level is above the vacuum level, as in Figure 3c. Therefore, in N.E.A materials one can have photoemission occur for energies lower than the bandgap, whereas in P.E.A. materials electrons require excitation energies in excess of their bandgap [2].

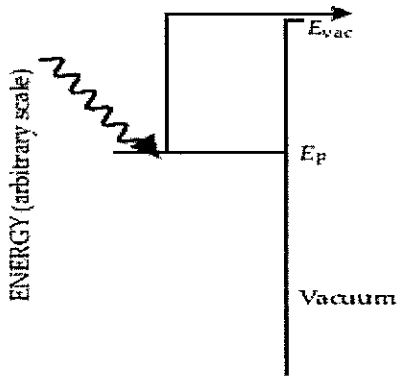

(a)

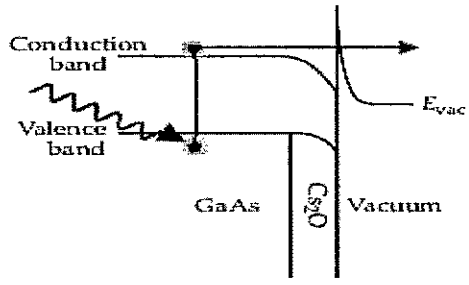

(b)

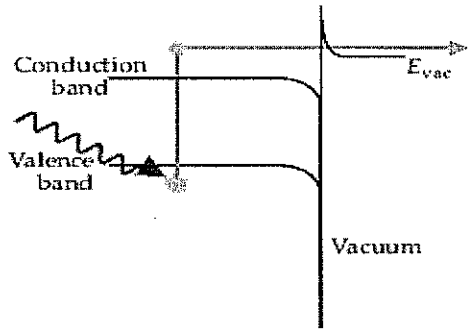

(c)

Figure 4: Photoemission from: (a) metals, (b) N.E.A films (c) P.E.A films [2].

2.4 Photoemission from Alkali Antimonides

The photoemissive properties of alkali antimonides have made them particularly useful in photodetector devices. In this regard, the more effective antimonides have been the alkali that possess two different alkali metals in their stoichiometry [8]. These antimonides with two alkali metals are therefore ternary compounds, in contrast to binary alkali antimonides that possess one alkali atom in their atomic structure. However, in either case both types of compounds have excellent absorptive properties in the visible light spectrum, 350nm to 780nm that make them highly suited to the emission of energy photons from this range. Another highly beneficial property from alkali antimonides, involves their ability to maintain their optical properties in either a solid or molten state [8]. The binary compound antimonide Cs_3Sb was discovered Gorlich, and the most notably relevant of alkali ternary compounds, Na_2KSb and K_2CsSb where both discovered by Sommer [9]. The processing of these compounds have traditionally required the initial deposition of an antimony layer. However a new approach was developed by a team at the Bhabha Atomic Research Center. With their technique there is no starting deposition of antimony and furthermore the thickness of the antimony layer is not monitored. Their basic approach was to begin by depositing potassium on a180°C phototube that acted as the substrate; antimony would only be evaporated onto the phototube after a little photocurrent was obtained. The Sb deposition was then continued in gradual amounts until a maximum photocurrent and hence maximum QE was obtained. At that point, if a K_2CsSb photocathode is required, then a co-deposition of cesium and antimony would be started and their

deposition rates adjusted so as to have a steady increase in photosensitivity until a peak was reached. On the other hand if a Na_2KSb cathode was desired, the initial k-Sb layer would be activated by a with sodium at 200°C until a rollover in photocurrent – then a co-deposition of potassium and antimony would follow until a new peak in photosensitivity was reached. Finally if a Na_2KSbCs photocathode was to be grown then the last procedure would be further followed by an addition of cesium with the substrate cooled to 160°C. Once the maximum sensitivity was achieved, a co-deposition of Cs and Sb would occur to obtain the highest photosensitivity possible [9]. The spectral response results of these main alkali antimonide photocathodes produced by this team can be seen in Figure 5 below.

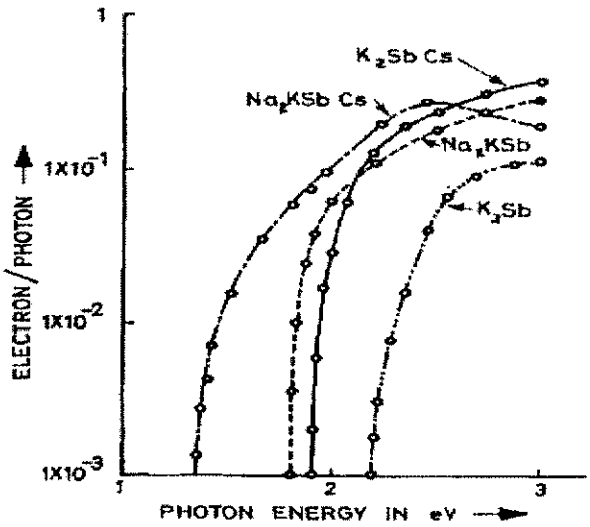

Figure 5: Spectral response curves versus photon energy [9].

Their spectral response results make it very evident that cesium potassium antimonide has the greatest peak current at photon energy greater than 3eV. The alkali antimonide films are semiconductors that possess unique bandgap properties. The Bhabha Atomic Research Center team also carried out

photoconductivity experiments to find the bandgaps of their grown antimonides. The approach of the team and their experiments, have helped provide evidence and insights into the critical aspects regarding growth of cathode films. These findings concluded that the sensitivity of the final film essentially was dependant on the initial potassium and antimony (K-Sb) layer. They found that their technique of starting with a potassium layer produced a photocathode with about an 18μA per meter higher sensitivity than with the conventional technique of initially depositing antimony. This result was attributed mainly to the exposure of the antimony layer to atmospheric residual gases enclosing the substrate. This occurs during the transition time from when the Sb layer is deposited, to the time that the K deposition commences. The team arrived at this conclusion after conducting electron microscopy experiments to examine the properties of the antimony layer under low-, high- and ultra-high vacuum conditions – when deposited in the conventional method. Their examination of the antimony layer revealed part of the crystal formation processes were involved during deposition onto a carbon substrate. The study revealed that antimony settled on the substrate in separated globules that enlarged until they "coalesced abruptly [9]" to form a molten and "electrically continuous film [9]". The first important characteristic that was noted was that the thickness at which coalition of the antimony layer occurred had a correlation with the vacuum quality. In particular they found that the antimony film required an additional 20 Angstrom growth to reach the coalition point. Furthermore, following the coalition, it is expected that the molten layer will crystallize. However, it was found that the crystallization process would

not even occur unless an ultra or, at minimum, a high vacuum was present. Therefore, the only logical explanation is that the presence of the residual gases in the chamber, especially at increasingly higher pressures has a negative impact on the coalition and crystallization process. A possible explanation of this, as expressed by their work, is that there are possible reactions of these gases with the antimony film before the globules, or "isolated islands [9]" are able to unite. An example is the oxidation of antimony atoms before deposition of potassium. Also notable was the hypothesis that deposited globules may vary in thickness and hence trap ambient gases either within the Sb layer or between the K-Sb interface. And finally, there was also strong concern for non-uniformity in the K-Sb layer. The reason was that the surface of the substrate is relatively large and hence the deposited antimony globules may not cover the entire surface. This would leave a region uncovered that would only have potassium deposited onto that region. They also found that the shear thickness of the antimony layers – stated as 300 Angstroms for the conventional method, meant that the potassium would be more concentrated in the outermost regions of the deposited antimony. Therefore, they concluded that the K-Sb sensitivity would be inhibited by these effects, and hence their approach using their co-deposition method would avoid this problem completely. When describing the growth of all their various alkali antimonide films each stage of deposition utilizes a simultaneous vaporization and thus the elements are more likely to have a correct gaseous mixture to create a more even composition in the film as they settle on the substrate. There is virtually a

guarantee that ambient vacuum gases will not be trapped between the two adjacent layers during a sequential deposition [9].

Regarding the bandgap research that was conducted the team, photoconductivity measurements [9] were utilized to get estimates of the bandgap energy values for the films grown using their technique. These results were tabulated in Table1.

Table1: Bandgap, threshold energy and electron affinity data [9].

Photocathode	Band gap	Threshold energy	n	Electron affinity
K_3Sb	1.8	2.2	1.28	0.4
K_2CsSb	1.2	1.9	1.08	0.7
Na_2KSb	1.1	1.8	1.35	0.7
$Na_2KSb(Cs)$	1.1	1.34	0.94	0.24

The premise for the bandgap energy values that are displayed in this table, is that the photon energy at which the photoconductivity of the photocathodes would stop increasing rapidly, would be the estimate of the semiconductor's bandgap energy. Varma and Ghosh also included threshold energy values, and electron affinity values for photoemission from their grown films. This was based on an equation that relates the quantum yield (Y) the incident photon energy (E) and threshold energy itself (E_t) as follows: $Y \sim (E - E_t)^n$; where n was a constant based on mode of excitation and scattering [9]. These results can be used as an approximation to the range of the bandgap energy that can be expected after a successful alkali antimonide film growth. Of the most interest to this research is the 1.2 eV bandgap, which is relatively close to that of GaAs (1.46eV). A

property of alkali antimonide that is commonly understood and reiterated in Varma's research is that they are extrinsic semiconductors - due to the addition of "impurity atoms" to the initial semiconducting element to alter its photoelectric properties. Varma and Ghosh's study also showed a relation between the film temperature and the photoemission at the threshold. In particular they found that a reduction of the film temperature at the threshold energy resulted in a reduction of the photoemmision [9]. They also found a considerable large reduction in the photoemission as their multialkali films were cooled from room temperature down to 90 Kelvin. The reason proposed for this phenomenon is that there is photoemission from the defect levels in the semiconductor that adds significantly to the overall emission. Hence, the activation energy levels of these levels were found by studying the electrical conductivity correlation to temperature at low temperature ranges [9]. Their findings are shown in Figure 6 where the logarithmic conductivity values are plotted versus inverse temperature (1/T) ranges in the Kelvin scale. In the plot the slope is taken to be $1/2\Delta E$ [9].

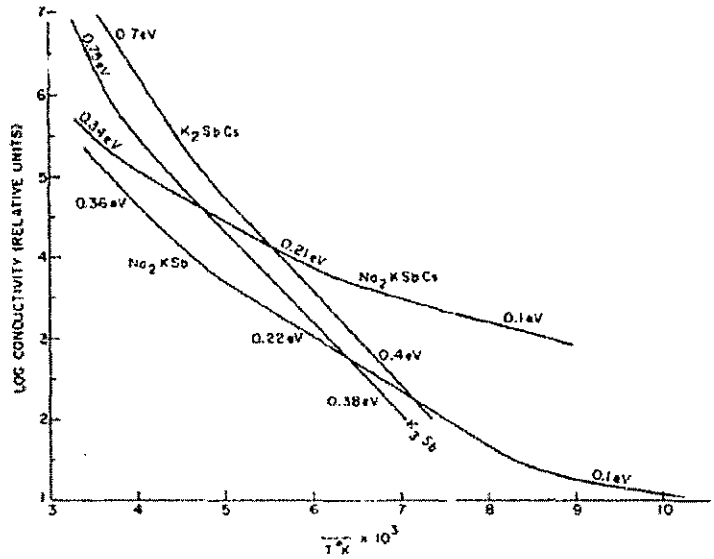

Figure 6: Logarithmic conductivity data for some grown alkali antimonides [9].

The plot can be assumed to give information concerning the defect levels because at these lower temperatures the Fermi level is expected to lie between the defect levels and "nearest band" [9]. The highlight from the plot regarding cesium potassium antimonide is that it has two distinct activation energies of 0.7eV and 0.4eV. Varma's study also discusses the importance of cesium in the multialkali antimonides. Conventionally, it had been assumed that a monolayer of cesium on top of the initial film materials reduces the electron affinity, i.e. surface barrier, of the photocathode substrate crystal. This was based on findings that the absolute amount of Cs was very small and that the optical absorption and crystal structure of Na_2KSb were not changed by the addition of Cs. However, work by Galant and Bates [10] to study the structure of multialkali antimonide photocathode from x-ray photoelectron spectroscopy (XPS) shows that the

thickness may be greater than a monolayer. In their work "a calculation using Cs 3p, 3d, 4d relative intensities, assuming Cs is only in a surface layer of thickness D, gives values for D from 15 to 95Å, with an average value of D~30Å [10]".

The XPS work of Galan and Gates [10] reveals a great deal of structural information regarding $Na_2KSb(Cs)$ (S-20 photocathodes). Their most significant finding was that the $Na_2KSb(Cs)$ structure consists of a heterojunction structure, where the base layer consists of bulk Na_2KSb and the top layer of K_2CsSb. The reasoning behind this is along the following lines: "In the last stage of S-20 processing, when CS and Sb are deposited on a photocathode formed by NaK_2Sb over Na_2KSb, one can expect diffusion of all the elements, with rates decreasing from CS,K, Na to Sb. The formation of new phases should also be expected. The possible phases are: Na_2KSb, NaK_2Sb, K_2CsSb, Na_2CsSb and Cs_3Sb. The two first ones seem unlikely in the surface layer after CS deposition. Cs_3Sb is probably unstable in the presence of K and Na; both Dowman *et al* (1975) and Dolizy *et al* (1977) did not detect the Cs_3Sb phase in any S-20 photocathode, and it is very well known that both Na and K easily displace Cs (Kansky1972). Hence, it seems reasonable to expect the formation of K_2CsSb and Na_2CsSb in the surface layer [10]". The heterojunction structure is illustrated in Figure 7. NaK_2Sb has a hexagonal structure, and is an n-type semiconductor that remains stable under an alkali excess – contrary to cubic alkali antimonides such as Na_2KSb, K_3Sb, and Cs_3Sb that have a very definite composition which are unstable under excess alkali presence. Furthermore, hexagonal alkali antimonides have lower alkali diffusion rates in comparison to cubic ones. K_2CsSb is cubic but shares

some properties of the hexagonal crystals; it has stability under conditions of excess the alkali and has low alkali diffusion rates due to low concentration of alkali vacancies [10].

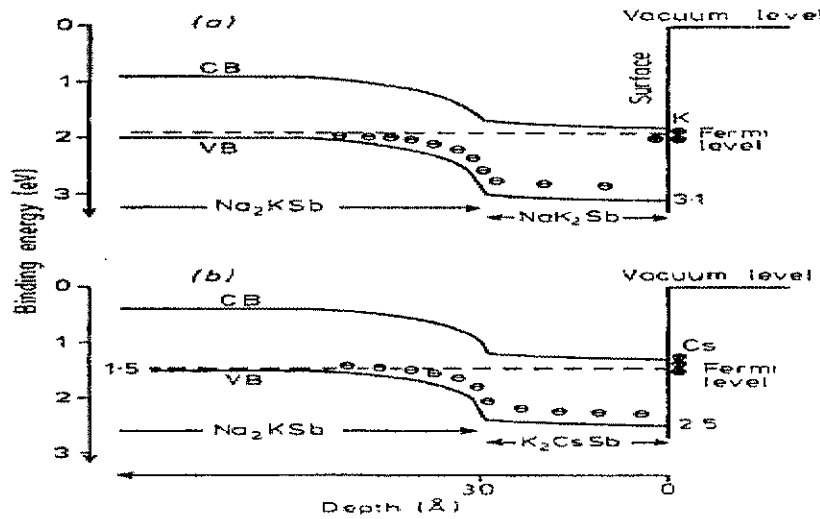

Figure 7: Heterojunction model of $Na_2KSb(Cs)$ [10].

2.5 Material Choice and Optical Properties of Alkali Antimonide Elements

In recent fabrication of alkali antimonides, cesium, potassium and antimony have been the material of choice based on several physical properties that promote easier fabrication as well as favorable optical properties within the visible spectrum. For example, in the fabrication of cesium potassium antimonide, the metalloid antimony has traditionally been the first element to be deposited in what has been called the "conventional method". Antimony melts at approximately 630°C and boils at around 1,587°C. Its boiling temperature at standard room temperature and pressure is much higher than those of potassium and cesium. Potassium has a melting point of 63°C and boils at 759°C and cesium melts at 25°C and 671°C. This higher melting temperature, in the conventional

technique, avoids initially depositing of cesium or potassium before antimony. Theoretically, depositing potassium or cesium and then ramping up to a higher temperature to achieve a molten physical state for antimony would likely cause the migration of the cesium and potassium species initially.

Regarding optical properties, the workfunction of antimony is approximately 4.55eV [11], therefore the approximate wavelength that can be utilized for illumination and photoemission can be found in the following way:

$$\lambda = \frac{hc}{eE}, \tag{5}$$

where λ is the illumination wavelength, h is Plank's constant of 6.626 x 10^{-34} Js, c is the speed of light equal to 3x10^{8} m/s, e is the charge of an electron equal to 1.602 x 10^{-19} C, and E is the workfunction energy in electron volts (eV). From this equation, one can estimate the wavelength of light required to 270nm.

The optical properties of alkali metals, in general, are quite unique and a number of these properties were studied by R.W. Wood of Johns Hopkins University [12]. The thin films of alkali metals are found to be opaque to visible light, but "highly transparent in the ultraviolet region [12]". Wood found that "the point at which the transparency commences moves towards shorter wave-lengths with decreasing atomic number as follows: Cs 4400Å; Rb 3600Å, K 3150 Å; Na 2100 Å; Li 2050 Å. According to Wood, this transparency to ultraviolet light continued as far down as his investigations had explored – reaching a wavelength of 1,860 Å.

In this ultraviolet region, a phenomenon known as "plane polarization by reflection" is observed – which produces plane polarized light by reflection of ordinary light at a Brewsterian angle. In Wood's work measurements of the reflection powers of these metals were conducted. The refractive index of potassium was also calculated using these measurements and from the Brewsterian angles for plane polarization, was found to be between 0.9 and 0.5 at wavelengths of 2,147Å and 3,100Å, respectively. With this value being less than unity total reflection would take place. Also, an estimation of film thickness was possible due to "interference maxima and minima in the spectrum of light reflected from the metal [12]". The deposition of these alkali films was conducted at liquid air temperatures. Liquid air temperature refers to very low temperatures, often also referred to as cryogenic, which is as low as -150C. These cryogenic temperatures were utilized to prevent a "colloidal deposit", which have different properties than the homogenous deposited films.

The results from Wood's study are seen illustrated in Figure 8, which shows the transmission spectra of the five studied alkali metals. The source of the light in these experiments was an end-on hydrogen tube with its inner walls silvered to suppress the line spectrum by catalyzing the atomic hydrogen [12]". The results of the reflecting power of the various films and the dispersion curve for potassium is displayed in Figure 9, and finally, the refractive index values found by Wood are tabulated in Table 2.

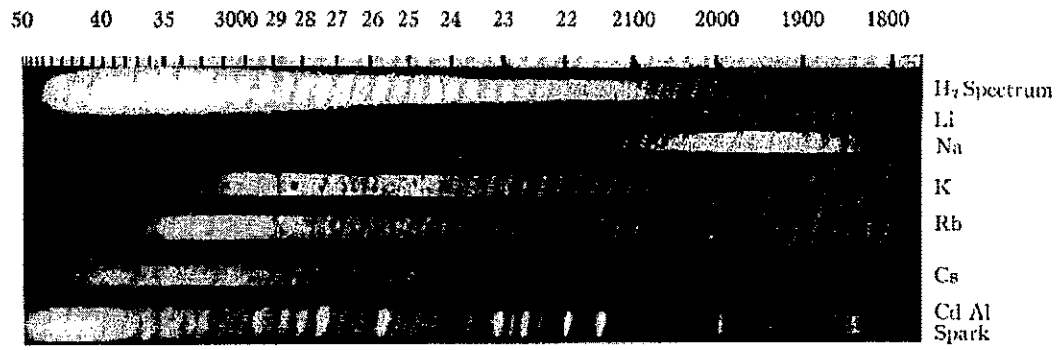

Figure 8: Transmission by alkali metals from hydrogen tube light source [12].

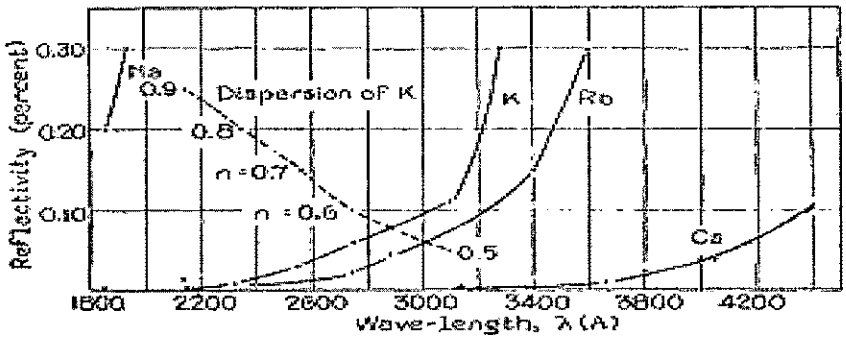

Figure 9: Reflecting power of films of alkali metals and dispersion curve for potassium [12].

Table 2: Refractive index of K film measured by reflection and by polarizing angle [12].

λ	n (from R)	n (from Pol)
2147	0.895	—
2200	.877	0.86
2314	.83	.80
2572	.70	.69
2748	.60	.58
3100	.50?	—

2.6 Cesium Potassium Antimonide

Of all the various multialkali antimonides that have been grown, cesium potassium antimonide has shown the most promise for future high current accelerator operations. The cesium potassium antimonide film grown for the injector purposes requires that it fulfills a number of requirements in the gun. As described by Pagani and Michelato, the general requirements of laser driven radio frequency (RF) gun include a fast response time. This usually allows the cathode to be called a prompt emitter by emitting and then ceasing emission as closely as possible to the on and off state of the incident laser. Furthermore, the cathode must have a high current density, greater than $500A/cm^2$. It should also preferably, have a good lifetime usually around a few hours, and finally, also a have a small field emission output in the applied field [13].

As noted earlier in the chapter, the presence of an extremely good vacuum, i.e. ultra high vacuum, is essential to a defect-free grown film. In Pagani's study, the partial pressures of the water, carbon monoxide, carbon dioxide, methane (CH_4), oxygen and nitrogen are prescribed to be kept below 10^{-12} mBar range [13]. An interesting aspect of the Cs-Sb layers discussed in Pagani's work is that the Cs and Sb reaction is irreversible in the case of multialkali cathodes, due to the chemical reactions between the elements within the layers [13].

Ternes and Bethel [14], Boeing Defense and Space researchers, carried out fabrication experiments to grow cesium-potassium antimonide cathodes. They utilized a $3x\ 2^{4-1}$ fractional factorial statistical experiment design to

"simultaneously determine the effects of five processing variables [14]" aimed at improving quantum efficiency. The investigated variables were antimony thickness, potassium thickness, source temperature, cesium temperature ramp down and substrate temperature. The team completed 35 combinations of the variables followed by another twelve-run "complementary phase [14]" that resulted in a total of 47 cathodes and estimates of the effects of these variables.

Specifically, these five variables were manipulated in the following ways: "(1) Substrate temperature (100°C without ramping, 140°C with ramping, and 160°C without ramping). (2) Antimony thickness (200°C and 1000°C). (3) Potassium thickness (200°C and 600°C). (4) Source temperature (all sources high and all sources low, where the low levels for antimony, potassium, and cesium were 480°C, 580°C, and 570°C, respectively, and the high levels were 520°C, 650°C, and 600°C, respectively). (5) Cesium temperature rampdown (yes or no) [14]." Therefore, it is apparent that the substrate temperature variable, and presence or absence of ramping is studied in combination. Also, by having all their sources at either a high or a low temperature setting, their results did not account for independent source temperature variation for each of the sources. Furthermore, the team realized that their sources depleted in a shorter period than expected. They, therefore, had to alter the chamber environment to install a second set of sources and eventually a third. A geometric representation of their preliminary approach is presented in Figure 10. In this figure they represent the first source with a shaded circle symbol and the second source with a shaded

square. The various combinations of these symbols on the corners of the cubes illustrate the combination of variables and their levels during experimentation.

The QE for their experiment was measured using a 543.5nm HeNe laser with a "total power of 930μW, and which delivers approximately 490μW to the cathode [14]", and a -90V bias was applied to the substrate. According to thesis work, they relate photocurrent and QE by using the equation $QE = jh\nu/eF$, where, $h\nu$ is the incident photon energy in Joules, F is the incident laser power density in Watts/cm^2, j is the current density in Amps per cm^2, and e the electron charge in Coulombs(C). By the conclusion of the work by Bethel, 47 cathodes had been fabricated. The QE data for all 47 films were plotted as seen in Figure 11. The results from the plot show that the "140°C with ramping" substrate temperature setting yielded superior average QE over the "100°C without ramping" substrate setting [14]. A summary of their measured QE for the various runs is also displayed in Table 3.

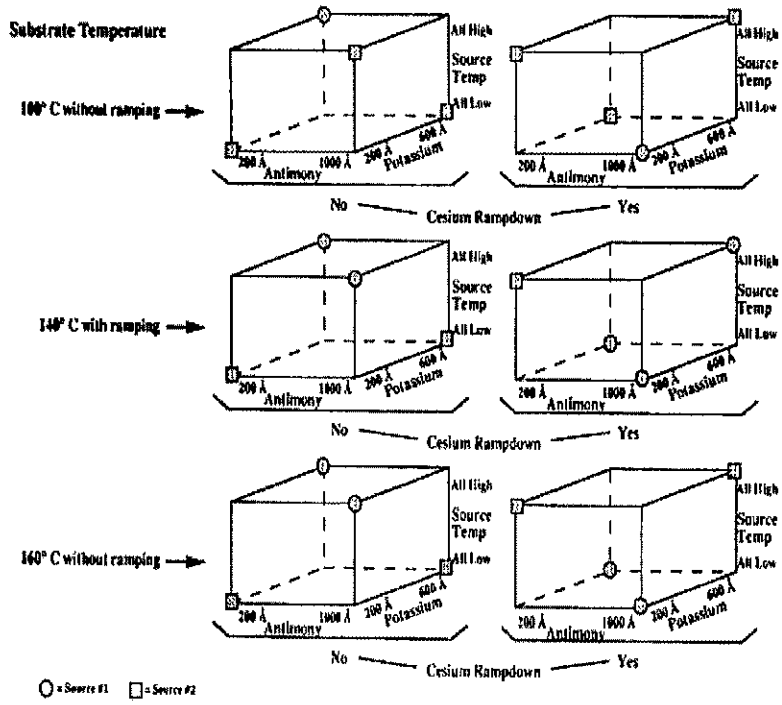

Figure 10: Geometric representation of Bethel [14] experimental approach.

The analysis of their data was performed using an "analysis of variance (ANOVA), a well-known method for modeling the variation in the data as a linear combination of components (effects) due to each of the factors (and their interactions) and due to random variation [14]". Generally, statistical tests (F-tests) were performed to find a probability value (*p*-value) relating associated with a particular variable level. And the lower the resulting *p*-value the "less likely the observed effect was due to chance alone [14]". A summary of this analysis is shown in Table 4. From this analysis they found that the only variable that had statistical significance was substrate temperature with a *p*-value of 0.0003. Furthermore, 140°C with ramping setting allowed them to reach the best average

QE of 6.1%. However, Ternes and Bethel also reiterate that the variations in the sources they utilized "results in statistically biased (to varying extents) [14]".

Table 3: Bethel experimental results summary for initial 47 cathodes [14].

Run	Substrate temperature	Antimony	Potassium	Source temperatures	Cesium rampdown?	Source	Quantum efficiency
1	160°C without ramping	200 Å	600 Å	all high	no	1	0.5
2	100°C without ramping	200 Å	600 Å	all high	no	1	1.0
3	100°C without ramping	1000 Å	200 Å	all low	yes	1	0.0
4	160°C without ramping	1000 Å	200 Å	all low	yes	1	0.0
5	130°C with ramping	1000 Å	200 Å	all low	yes	1	2.3
6	130°C with ramping	200 Å	600 Å	all high	no	1	3.8
7	140°C with ramping	200 Å	600 Å	all low	yes	1	7.6
8	140°C with ramping	1000 Å	200 Å	all high	no	1	0.8
9	160°C without ramping	200 Å	600 Å	all low	yes	1	0.0
10	160°C without ramping	1000 Å	200 Å	all high	no	1	0.0
11	100°C without ramping	1000 Å	200 Å	all high	no	2	2.6
12	100°C without ramping	200 Å	600 Å	all low	yes	2	4.3
13	140°C with ramping	1000 Å	600 Å	all low	no	2	10.6
14	160°C without ramping	200 Å	200 Å	all high	yes	2	0.0
15	100°C without ramping	1000 Å	600 Å	all low	no	2	0.4
16	100°C without ramping	200 Å	200 Å	all high	yes	2	6.4
17	140°C with ramping	200 Å	200 Å	all high	yes	2	9.7
18	160°C without ramping	1000 Å	600 Å	all low	no	2	0.0
19	100°C without ramping	200 Å	200 Å	all low	no	2	2.5
20	160°C without ramping	1000 Å	600 Å	all high	yes	2	0.0
21	140°C with ramping	1000 Å	600 Å	all high	yes	1	2.1
22	100°C without ramping	1000 Å	600 Å	all high	yes	2	3.5
23	140°C with ramping	200 Å	200 Å	all low	no	2	8.0
24	160°C without ramping	200 Å	200 Å	all low	no	2	0.0
25	100°C without ramping	1000 Å	200 Å	all low	yes	3	1.5
26	100°C without ramping	200 Å	600 Å	all high	no	3	1.8
27	140°C with ramping	1000 Å	600 Å	all high	yes	3	9.8
28	140°C with ramping	1000 Å	600 Å	all low	no	3	7.0
29	140°C with ramping	200 Å	200 Å	all high	yes	3	6.4
30	100°C without ramping	200 Å	600 Å	all low	yes	3	2.4
31	140°C with ramping	200 Å	200 Å	all low	no	3	7.4
32	100°C without ramping	1000 Å	200 Å	all high	no	3	0.3
33	140°C with ramping	1000 Å	200 Å	all high	no	3	2.7
34	140°C with ramping	200 Å	600 Å	all high	no	3	3.4
35	140°C with ramping	200 Å	600 Å	all low	yes	3	7.7
36	140°C with ramping	200 Å	600 Å	all low	no	3	6.1
37	140°C with ramping	1000 Å	200 Å	all high	yes	3	0.8
38	140°C with ramping	200 Å	200 Å	all low	yes	3	2.5
39	140°C with ramping	200 Å	600 Å	all high	yes	3	1.2
40	140°C with ramping	200 Å	600 Å	all low	no	4	1.2
41	140°C with ramping	1000 Å	200 Å	all high	yes	4	2.3
42	140°C with ramping	200 Å	200 Å	all low	yes	4	2.6
43	140°C with ramping	200 Å	600 Å	all high	yes	4	2.8
44	140°C with ramping	1000 Å	200 Å	all low	no	4	1.5
45	140°C with ramping	1000 Å	600 Å	all low	yes	4	2.5
46	140°C with ramping	1000 Å	600 Å	all high	no	4	1.9
47	140°C with ramping	200 Å	200 Å	all high	no	4	0.8

Table 4: Analysis of variance of average QE for 35 runs [14].

Source	df	SS	MS	F	P
Source	2	21.8	10.9	3.5	0.0623
Substrate temperature	1	77.3	77.3	25.0	0.0003
Antimony thickness	1	13.4	13.4	4.3	0.0597
Potassium thickness	1	1.3	1.3	0.4	0.5215
Source temperature	1	0.2	0.2	0.1	0.8168
Cesium temperature rampdown	1	18.1	18.1	5.9	0.0323
Antimony thickness*potassium thickness	1	3.7	3.7	1.2	0.2942
Antimony thickness*source temperature	1	0.3	0.3	0.1	0.7628
Antimony thickness*cesium temperature rampdown	1	0.7	0.7	0.2	0.6409
Substrate temperature*antimony thickness	1	0.8	0.8	0.3	0.6102
Substrate temperature *potassium thickness	1	7.2	7.2	2.3	0.1538
Substrate temperature*source temperature	1	15.8	15.8	5.1	0.0432
Substrate temperature*cesium temperature rampdown	1	0.6	0.6	0.2	0.6786
Residual	12	37.1	3.1		

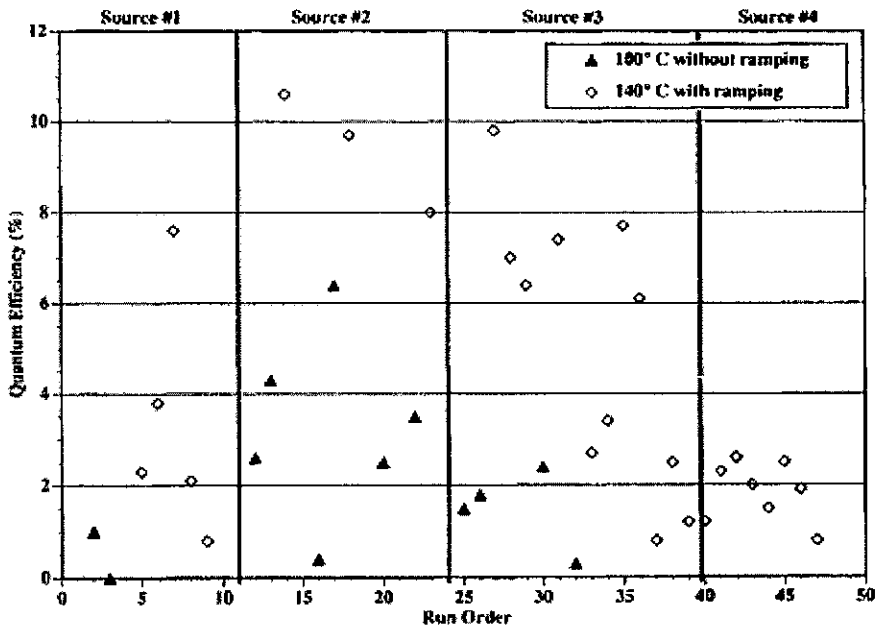

Figure 11: QE versus run order of the 47 photocathodes.

As noted by Gates [10] K_2CsSb is cubic but shares some properties of the hexagonal crystals, and having a low concentration of alkali vacancies allows it to be easily alkali – doped to form an n-type material. According to Gates the

properties that make K_2CsSb an optimal overlayer in the formation of $Na_2KSb(Cs)$ is its large lattice constant resulting in "a small valence band binding energy, and hence a small real photoemission threshold". Its bandgap has been found to be between 1.2 and 1.4eV [9] [10].

K_2CsSb has been primarily pursued as an accelerator photocathode due to its high average current output. Demonstrating this high current ability is the fact that it has been the only cathode to have produced average current of 35mA in an accelerator environment. Brookhaven National Laboratory (BNL) has been conducting cathode research to find an optimum photocathode for their energy recovery linac (ERL). An ERL is generally "a new type of synchrotron radiation machine, based on a superconducting linac and a one-turn return arc (like a storage ring) [15]". A similar endeavor to construct an ERL is underway at Cornell University, funded by the National Science Foundation (NSF) to the amount of 18 million dollars [15]. At BNL the grown cathodes have been tested on two substrate materials copper and stainless steel. The lifetime of K_2CsSb has been measurable in terms in time units of hours for a normal-conducting (NC) RF cavity which has a relatively poor vacuum of (~1nTorr). However, this lifetime may be further increased in a superconducting (SRF) injector where a vacuum of up to $\sim 10^{-11}$Torr can be obtained [16].

These properties of K_2CsSb are evidenced by some experimental results achieved by BNL. Their results are based on four grown cathodes in a ~0.02nTorr vacuum environment. The K_2CsSb cathodes were grown on the aforementioned substrates using a vertical sequential deposition method as adopted by Dowell

[17]. With this method the three elements antimony, potassium and cesium are deposited on the substrate located 2.5cm above these sources. A positively biased anode sets up an electric field to extract current from the cathode, which is illuminated with a 532nm green laser. The spectral response results for their second cathode are displayed in Figure 12. As seen from the plot, the high current and hence highest QE at a wavelength of 532nm is obtained using the stainless steel substrate.

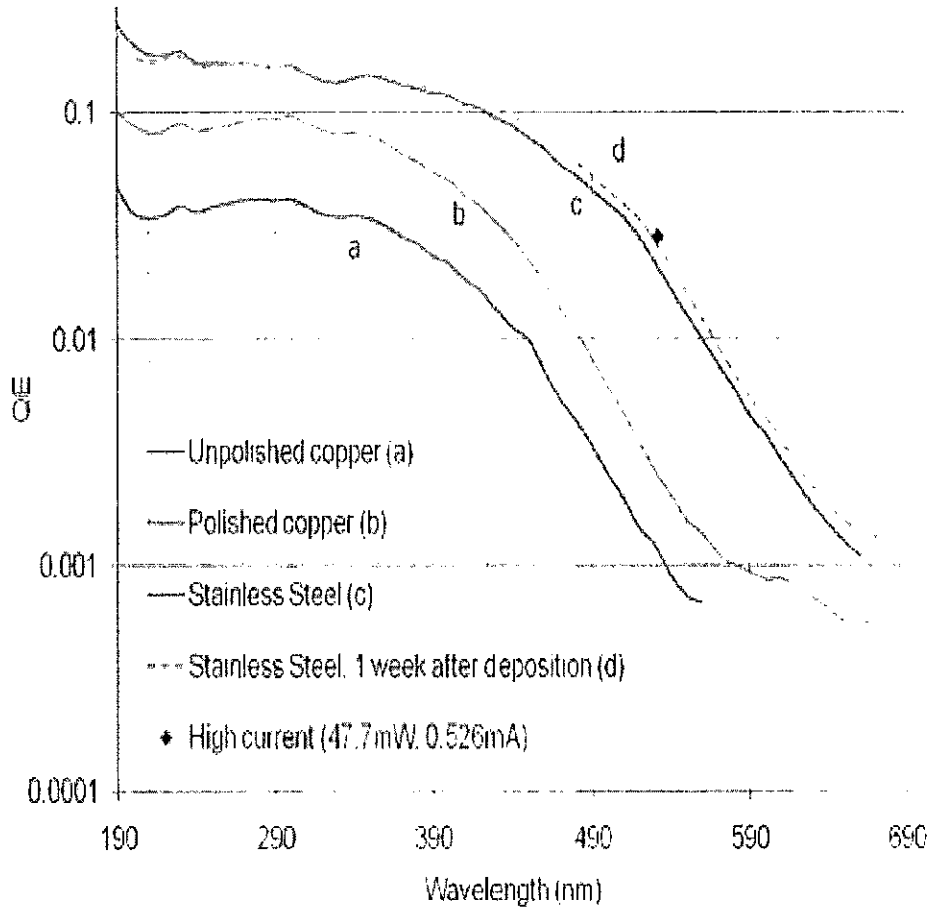

Figure 12: BNL spectral response of K_2CsSb versus wavelength for 4 substrates [16].

2.7 Quantum Efficiency and Lifetime

The quantum efficiency property is associated with semiconductor films that undergo photoelectric effects in the presence of electromagnetic radiation on their surface. Quantum efficiency is defined as the number of electron-hole pairs generated for each incident photon [18]. The equation used to find the quantum efficiency is [18]:

$$\eta = \left(\frac{I_p}{q}\right)\left(\frac{P_{opt}}{h\nu}\right)^{-1}, \tag{6}$$

where I_p is the photocurrent generated from the absorbed optical energy, $h\nu$ corresponds to the photon energy, P_{opt} is the incident optical power, and q is the electron charge value of 1.6 $x10^{-19}$ C. This is equation can be reduced to the simpler form (shown below). In this form, the equation's frequency variable ν is substituted for the ratio of the velocity of light (c) over the wavelength λ, then the product of Plank's constant h and the velocity of light divided by the electron charge value produces a constant of 0.00000124. Furthermore, if the units of wavelength, λ are considered in nanometers (nm) and the units of power in milliWatts, then the constant may be expressed as 1.24. If the value is stated as a percentage then it can simply be expressed as 124 as in the final form of the equation below:

$$\eta = \left(\frac{124}{\lambda}\right)\left(\frac{I_p}{P_{opt}}\right) \tag{7}$$

The lifetime of the photoemissive film, in terms of the quantum efficiency property, is another property of interest. The quantum efficiency of the film

undergoes an exponential decay over time. Generally the process of decay can be described by a differential equation of the form shown below. The left side of the equation represents the decreasing rate of the quantum efficiency quantity, $-\frac{dQ(t)}{dt}$, at any given instant in time. It is related to the QE at the same instant in time, Q(t). Therefore, the left side of the equation is referred to as the decay rate of the quantum efficiency. This rate is directly proportional to the quantum efficiency at a sample time. The constant of proportionality c, is called the decay constant. The lifetime, more formally known as the mean lifetime is then defined as the reciprocal of the decay constant. Therefore, lifetime $T_{lifetime} = 1/c$. The equation for the rate if change of quantum efficiency is:

$$-\frac{dQ(t)}{dt} = cQ(t) \tag{8}$$

Also, solving the above first-order linear differential equation yields the quantum efficiency for a sample time as $Q(t) = Q_o e^{-ct}$, where Q_o is the initial quantum efficiency or maximum quantum efficiency at the start of the experiment, that is, at time t = 0. The half-life is a quantity that refers to the length of time required for the initial value of the quantum efficiency to decay to half its original value. Therefore, the half-life can be defined in terms of the solved equation as $½ = e^{-cT}$, where T is the half-life. Hence: T = In2/c. Accordingly, the lifetime can be defined in terms of the lifetime as $T_{lifetime} = T_{1/2}/In2$.

2.8 Photoemission From GaAs versus Alkali Antimonides

Photoemission from GaAs has been well established on an industrial level and has been used to produce "high-efficiency photocathodes in the visible and near-infrared spectrum [19]." For a decade leading up to 1984 and to the present "negative-electron-affinity (N.E.A.) photocathodes have been used in photomultiplier tubes and the activation procedure, developed for industrial purposes, is well known [19]." Furthermore, under excitation from circularly polarized light, GaAs has applications in high-energy, molecular, atomic and surface physics. "It has been shown that GaAs provide intense and quasimonochromatic electron beams and in this way greatly improve the performance of available electron sources [19]". It is for these reasons that the GaAs, often p-type doped, has been the primary choice for electron sources. "Current research is directed toward increasing the polarization, bunch charge, average current, and cathode lifetimes. As briefly mentioned earlier, GaAs has what is known as a direct bandgap, which is one of two specific classes of semiconductors. That is, photosensitive semiconductors may be either direct or indirect semiconductors. Formally, direct bandgap semiconductors are defined as semiconductors that have the minimum of their conduction bands occurring at the same wavevector, k, as the maximum of their valence bands. Generally, these are known to have a "stronger absorption of light as characterized by a larger absorption coefficient [20]". Due to this property, direct bandgap semiconductors are favored when fabricating light emitting devices. On the other hand, "indirect bandgap semiconductors are semiconductors for which the minimum of the

conduction band does not occur at the same wavevector as the maximum of the valence band and are known to have a smaller absorption coefficient, and therefore and are rarely used in light emitting devices [20]". In terms of the absorption process, direct bandgap semiconductors can have the transition of an electron from the valance band to the conduction band without a change in momentum within the crystal. Hence, the transition only involves a photon. However, for indirect semiconductors the transition process requires not only a change in energy from an absorbed photon but also requires a phonon to assist in a change of momentum in the crystal [20]. These processes are illustrated in the energy versus k-vector or momentum curves shown in Figure 14. Specifically, Figure14a shows photon absorption in a direct bandgap semiconductor. Figure14b illustrates photon absorption in an indirect bandgap semiconductor, which is assisted by phonon absorption. Finally, Figure 14c displays photon absorption in an indirect bandgap semiconductor assisted by phonon emission.

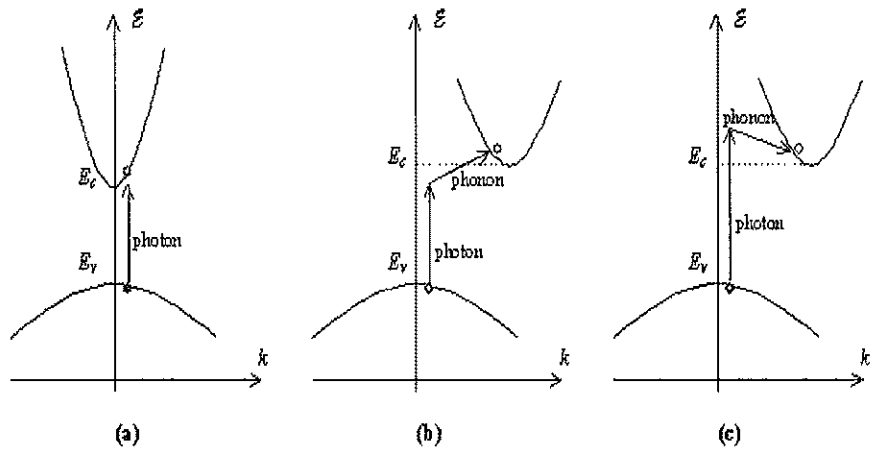

Figure 13: Photon absorption in direct and indirect semiconductors [20].

GaAs and cesium potassium antimonide semiconductor photocathodes are similar in that they are both direct bandgap semiconductors. Regarding photoemission and QE, K_2CsSb has been demonstrated to produce a QE of greater than 4% at 532nm and greater than 10% at 355nm [16]. This is comparable to GaAs that has been used to produce a 5% QE at 532nm at Jefferson Laboratory. Research experiments on alkali antimonides is aimed at eventually surpassing the 5% QE value at 532nm and shows promise for even greater current output using such a source.

CHAPTER III

EXPERIMENTAL DETAILS AND METHODOLOGY

3.1 Introduction

This chapter presents a full description of the apparatus, procedures and basic theory that were involved in the actual experimentation phase of the research. Section 3.2 gives a detailed description of the equipment that was used including: (1) equipment involved in establishing a vacuum environment, (2) the thermal sources that were utilized for the emission of film materials (two forms of sources were utilized as material vapor sources), and (3) monitoring equipment that was utilized to estimate the deposition rates and thickness of deposited materials. The sub-sections of 3.2.1 - 3.2.3 address general theory and the approach that was utilized to characterize the deposition rates and deposited thicknesses from the sources.

Section 3.3 gives a discussion of the standard methodology involved to produce the vacuum within the chamber, primarily the bake procedure; the heating cycle and the resulting vacuum curves plotted in terms of ion pump current Ip. Finally Section 3.4 provides an explanation of the sequentially-ordered method of producing the films deposited in each trial. There is also a description of how the setup and physical variables of the experiment were varied to gain data on effects of changing such properties. Furthermore, this section also includes information regarding the limitations involved in the procedures and the alternatives accessible for possible implementation if further experimental time

were available. Chapter 3 therefore is an excellent segue into Chapter 4; the conclusions and results portion of the thesis.

3.2 Experimental Equipment and Details

3.2.1 Vacuum Equipment

All experiments were carried out in a well-established high vacuum environment. This vacuum environment was created in a cylindrical stainless steel chamber that is illustrated in Figure 15. The cylindrical chamber has an internal diameter of 8" and a height of ~14". Therefore, the main chamber cavity holds a volume of approximately $\pi*4"^2*12" = 603in^3$. The vacuum chamber in its basic setup houses three $2^3/_4$" diameter source ports. The bottom of the chamber also has a $2^3/_4$" laser port window that provides a vertical line of sight into the center of the chamber. There is also one of two $4^1/_2$" ports that is used to house an anode ring. The ring is given a positive bias via a Bayonet Neill-Concelman (BNC) cable connected to a battery voltage supply unit. The second port is used as the input to the ion pump of the chamber. On the top of the chamber is a fifth $2^3/_4$ " port that is used to insert a 13" stainless steel, molybdenum-tipped stalk. The molybdenum tip serves as the substrate for all experiments. An image of the real-life chamber and setup for the experiments can be seen in Figure 16.

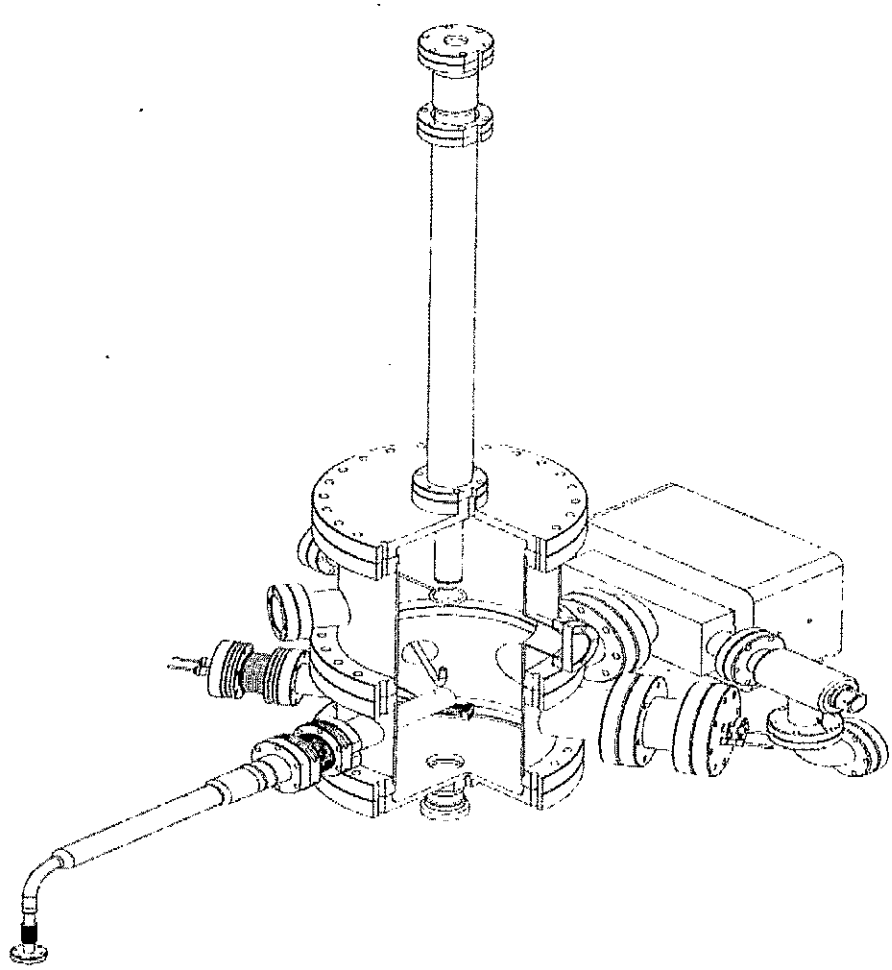

Figure 14: Schematic of vacuum chamber.

3.2.2 Monitoring Equipment

The experiment involved some properties that must be explored to optimize the quantum efficiency of the grown films. Therefore, to accurately grow the films in a reproducible fashion as well as to have a close idea of the how much material is deposited, various monitoring equipment was essential. To this end, mainly three forms of equipment were utilized. These included a thickness monitor, a laser power meter, an ion pump meter and multimeter.

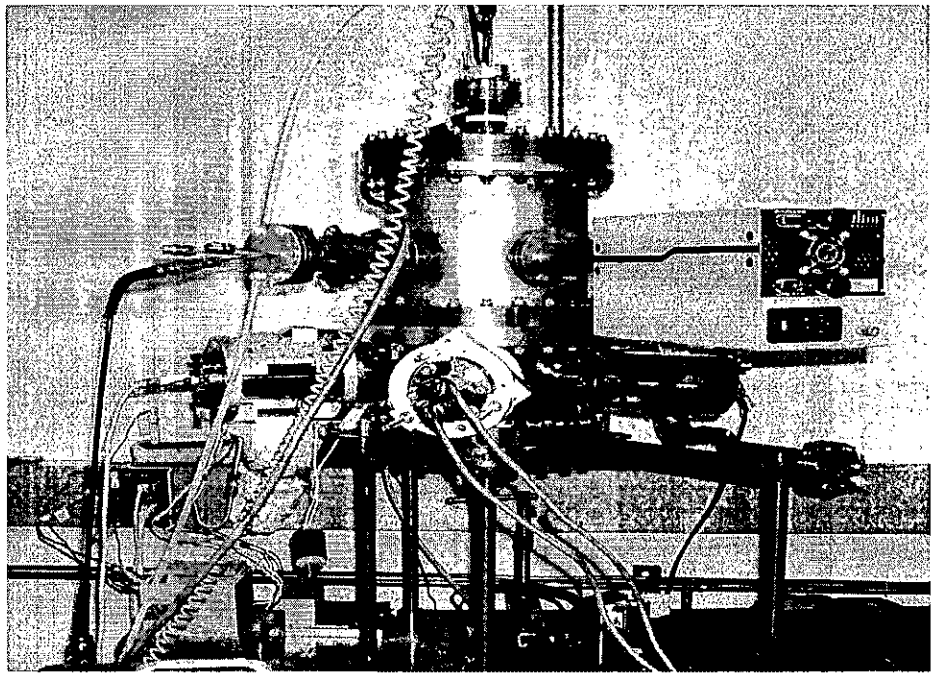

Figure 15: Image of actual experimental vacuum chamber.

The thickness monitor can be described as a sensor head, a schematic which is shown in Figure 17. Its function is to determine the thickness and rate of material deposition within the vacuum chamber. This sensor head is composed of a stainless housing and gold-plated crystal holder that snaps into the stainless housing. The stainless housing also includes a water cooling system that circulates water through the sensor head. The purpose of the crystal holder is to host a .550" diameter quartz crystal with an oscillating frequency of 6MHz. The sensor head is inserted into the chamber and faces downward towards the material sources. Generally, in the thickness monitor, the change in mass of quartz crystal as vaporized material collects on the crystal, results in a change in oscillating frequency of the crystal. This allows the determination of the thickness of deposited material. An external oscillator is excited into motion by an external

oscillator to 6MHz. The addition of material reduces this frequency, and the thickness is related to the frequency by the following equation:

$$TK = \frac{NqPq}{P_f f^2}(fq - f), \tag{9}$$

where TK is the thickness of deposited material, Nq is a frequency constant for an AT-cut quartz crystal (i.e. Y-axis cuts such that the top and bottom halves of the crystal move in opposite directions during oscillations) vibrating in the shear thickness mode (1.668 x 10^5m/s), Pq is the density of quartz in g/cm^3, fq is the resonant frequency of the uncoated crystal, f is the resonant frequency of the loaded crystal, and P_f is the density of the deposited film. The monitor is connected to a controller which provides a digital output of the rate of deposition and thickness of deposited material.

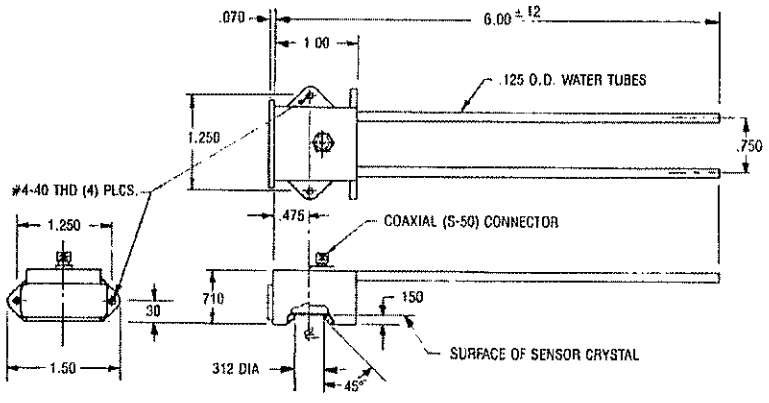

Figure 16: Thickness monitor sensor head schematic.

The thickness monitor controller requires several inputs to accurately record the thicknesses of materials being deposited. These include variables such as the density of the materials. Two critical inputs to the controller are the tooling

factor and the acoustic impedance of the materials. The tooling factor, is a percentage value that accounts for the geometric arrangement with regard to the thickness monitor sensor head and the substrate. It also accounts for the differences between the deposition rates on these two surfaces. The tooling factor is defined by the equation below:

$$Tooling\ \% = \left(\frac{dcry}{dsub}\right)^2 x\ 100\% \tag{11}$$

In the above equation, 'dcry' is the distance from the source to the crystal and 'dsub' is the distance from the source to the substrate. This relation is arises from the fact that the mass of material that is emitted from the source at a given intensity drops at a rate that is proportional to the inverse of the distance, typically donated r, from the source point. The acoustic impedance, or specifically the shear wave acoustic impedance, is required to allow the monitor to accurately account for the sensor scaling factor to compensate for being heavily loaded by vaporized material. This value is an input on the controller in units of 100,000 gm cm^{-2} s^{-1}. The Handbook of Physics is the typical reference for acoustic impedance values for different materials. The acoustic impedance can be calculated using the formula of Equation 12. According to this formula the impedance can be found either by using the density of the material (ρ) and the transverse (shear) wave velocity, C in units of cm/s or the shear modulus, G in units of dynes /cm^2. Table 4 gives the acoustic impedance values for several materials

$$Acoustic\ impedance = \rho C = \sqrt{\rho G}\ . \tag{12}$$

Table 5: Density and acoustic impedance values [21].

Material Name	Symbol	Density gm/cm^3	Acoustic Z $\times 10^5$ gm/cm^2 sec
Aluminum	Al	2.700	8.170
Aluminum Antimonide	AlSb	4.360	11.884
Aluminum Oxide	Al_2O_3	3.970	26.280
Antimony	Sb	6.620	11.490
Arsenic	As	5.730	9.140
Barium	Ba	3.500	4.200
Barium Flouride	BaF_2	4.886	11.135
Barium Nitrate	BaN_2O_6	3.244	7.002
Barium Titanate (Cubic)	$BaTiO_3$	6.035	21.432
Barium Titanate (Tetr)	$BaTiO_3$	5.999	19.030
Beryllium	Be	1.850	16.260
Bismuth	Bi	9.800	11.180
Boron	B	2.540	22.700
Cadmium	Cd	8.640	12.950
Cadmium Sulfide	CdS	4.830	8.660
Cadmium Telluride	CdTe	5.850	9.010
Calcium	Ca	1.550	3.370
Calcium Fluoride	CaF_2	3.180	11.390
Calcium Sulfate	$CaSO_4$	2.962	9.246
Carbon (Diamond)	C	3.520	40.140
Carbon (Graphite)	C	2.250	2.710
Cesium Bromide	CsBr	4.456	6.262
Cesium Chloride	CsCl	3.988	6.312
Cesium Iodide	CsI	4.516	5.726
Cesium Sulfate	Cs_2SO_4	4.243	7.285
Chromium	Cr	7.200	28.950
Cobalt	Co	8.710	25.740
Cobalt Oxide	CoO	6.440	21.432
Copper	Cu	8.930	20.210
Copper (I) Sulfide (alpha)	Cu_2S	5.600	12.800
Copper (I) Sulfide (beta)	Cu_2S	5.800	13.180
Copper (II) Sulfide	CuS	4.600	10.770
Dysprosium	Dy	8.540	14.720
Erbium	Er	9.050	11.930
Gadolinium	Gd	7.890	13.180

3.2.3 Sources and Source Characterization

The PVD sources used in the experiments of this research required characterization to understand the rate of substrate deposition that could be expected from each source. Therefore, estimation was required for the antimony, cesium and potassium source. The antimony source comprised of an alumina oxide crucible that sits inside a tungsten filament as seen in Figure 18. Antimony

pellets are used to fill the crucible, and these are resistively heated as current is run through the filament wire. Antimony (Sb) is a metalloid with a melting point of about 630C, and hence sufficient current must be passed through the filament to reach this temperature. The antimony pellets used in the experiments are of 99.99% high purity, as can be seen in the residual gas analyzer scans in Figure 20, the two isotopes of antimony, antimony 121 and 123 are elevated during evaporation.

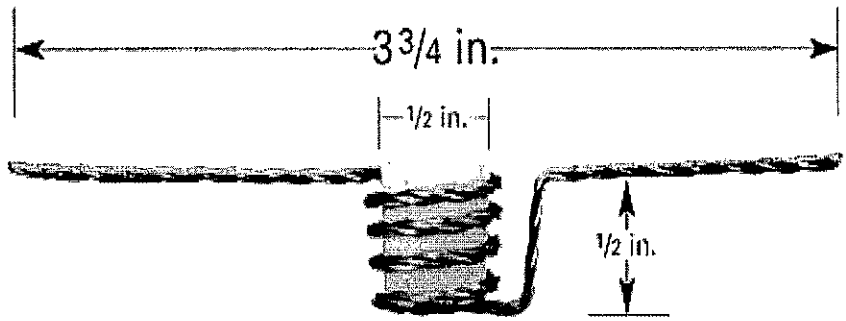

Figure 17: Alumina oxide crucible in tungsten filament [22].

The antimony source is characterized to gain an estimate of its deposition rate, and the substrate to thickness monitor deposition ratio. Experimentally this was conducted by placing a glass slide over the substrate surface and vaporizing antimony from the source over a period of time. The thickness monitor reading is recorded for the time interval. The Atomic Force Measurement (AFM) technique was then utilized to obtain a thickness estimate from the glass slide sample. The surface imagery of the deposited slide is shown in Figure 19. The corresponding profile measurement is displayed in Figure 20. The image indicates two primary measurement points with an average measurement of 14.2 nm (or 142

Angstroms). The ratio of recorded thickness monitor reading and the AFM measurement gives the monitor to substrate deposition ratio for the antimony source.

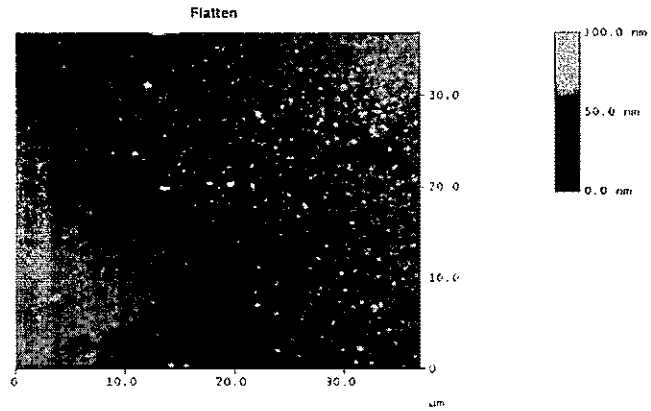

Figure 18: Glass slide antimony sample AFM image.

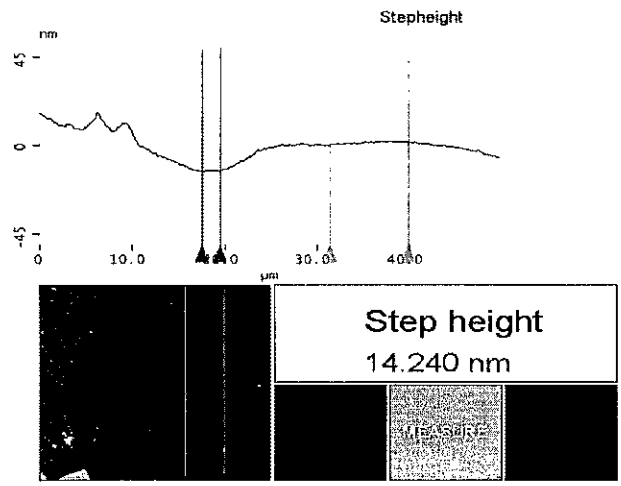

Figure 19: Antimony deposition sample AFM measurement.

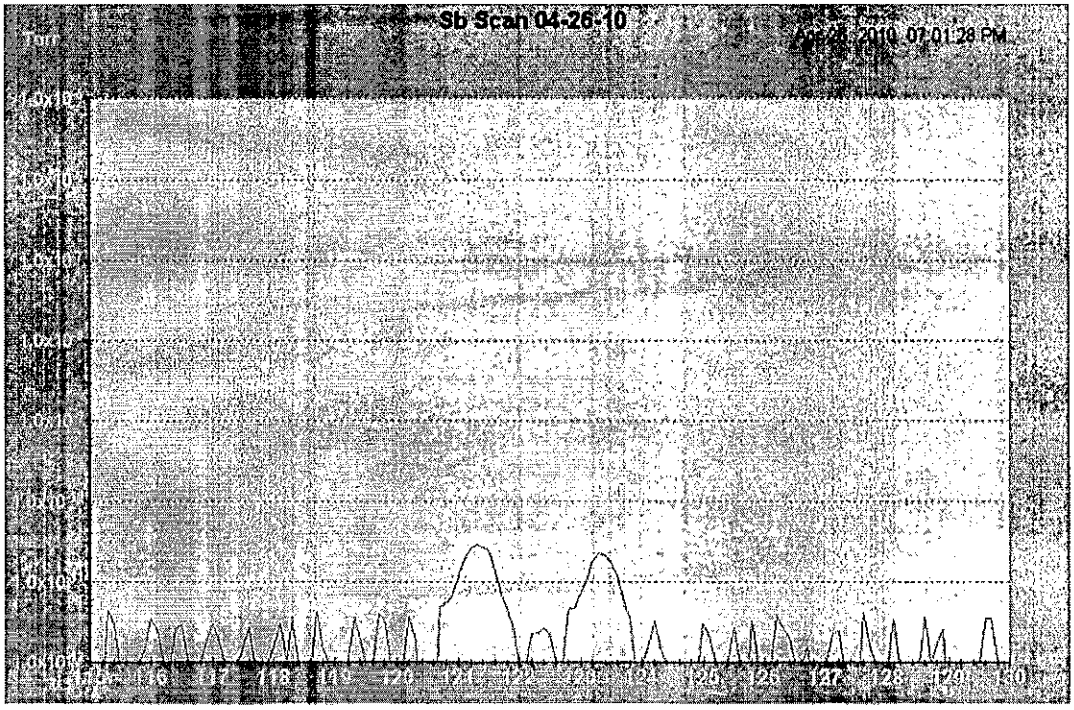

Figure 20: RGA scan of partial pressure peaks of antimony.

Two forms of sources were utilized for cesium deposition for two different setups. The first source, was in the form of alkali metal dispensers (AMDs). AMDs from SAES are alkali metal chromates mixed with a reducing agent used for photocathode fabrication [23]. "The chromates used are anhydrous alkali metal salts of chromic acid having the general formula Me_2CrO_4, where Me is the symbol used to indicate any one of the alkali metals (Cs, K, Na, Rb and Li) [23]". The reducing agent is an alloy called St 101 (86%-Zr and 16%-Al), and apart from the reducing action, it acts to absorb any other gases produced in the reduction reaction that would contaminate the alkali vapor. For SAES dispensers it is assumed that the metal vapor is released typically between 550 – 850C, however the higher the temperature of operation, the higher the rate of vaporization. The temperature of the dispensers can be controlled by the amount

of current run through the metal dispensers. In the experimental setup of this research, a current is passed through two copper rods electrically linked to two dispenser strips that are joined by a nickel conductor to form a circuit. The terminals of the rods are electrically insulated from the bellows through which they run. The bellows for each source allow the insertion and removal of the source from underneath the substrate at the center of the chamber. Figure 22 shows an RGA scan of a cesium pressure peak within the chamber from an activated source. The y-axis displays the vacuum pressure in Torr and the x-axis shows molecular weight values in grams per mole (g/mol). Figure 23 shows a similar RGA pressure peak for a K source: a potassium signal at mass 39 can just barely be discerned near the mass 40 peak (argon). Finally in Figure 24, a general chamber vacuum scan gives an idea of the vacuum condition in the chamber; the hydrogen pressure is seen to approach 10^{-7} Torr. Plots of the Temperature versus Current dependence of the dispensers as well as typical Yield versus Current plots for the Cs and K dispensers are shown in Figure 25 and Figures 26a and 26b, respectively.

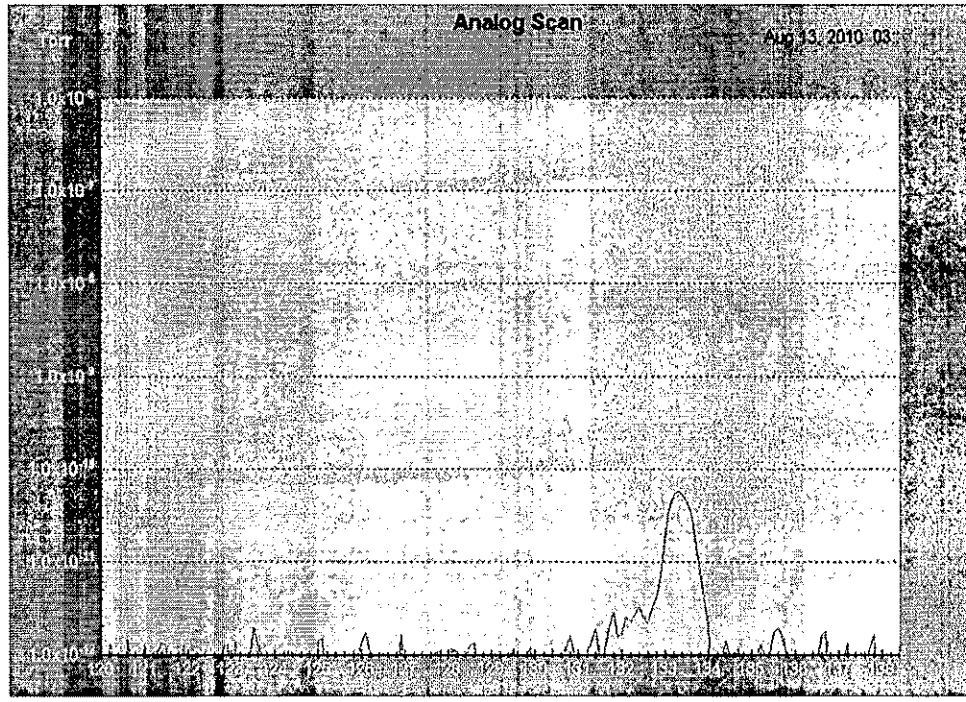

Figure 21: RGA scan of partial pressure peak of cesium (atomic mass 133g/mol).

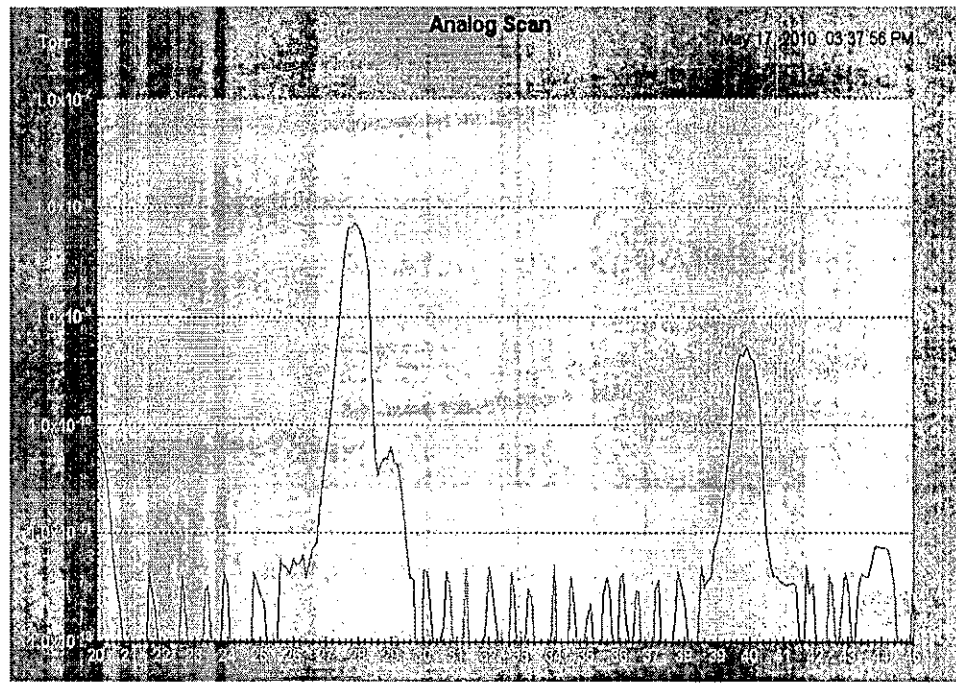

Figure 22: RGA scan of partial pressure peak of K (atomic mass 39g/mol).

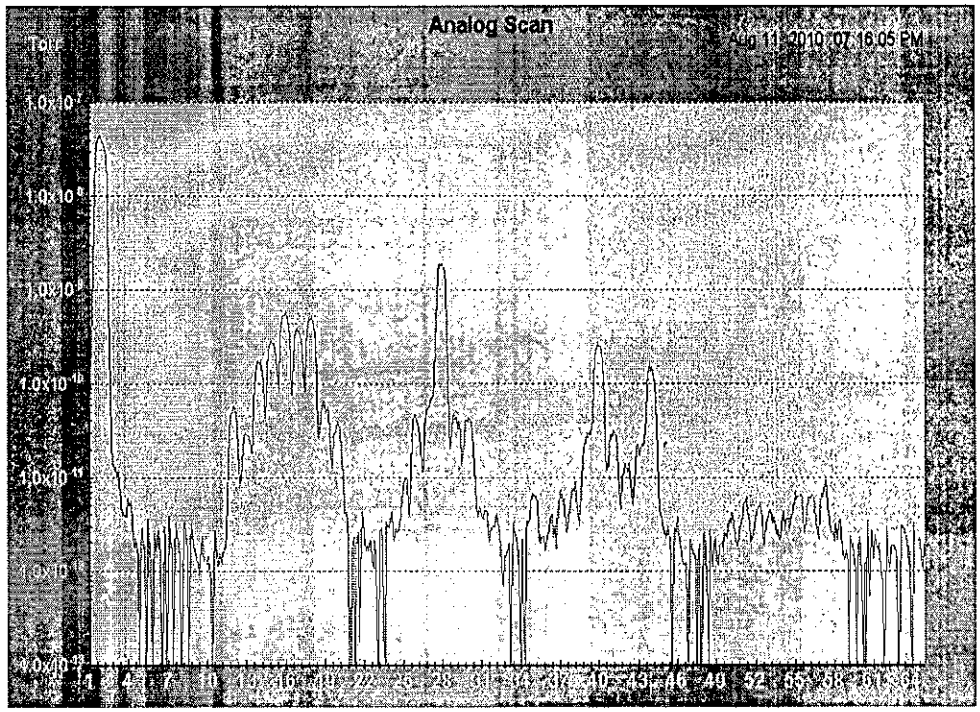

Figure 23: RGA scan of general vacuum status.

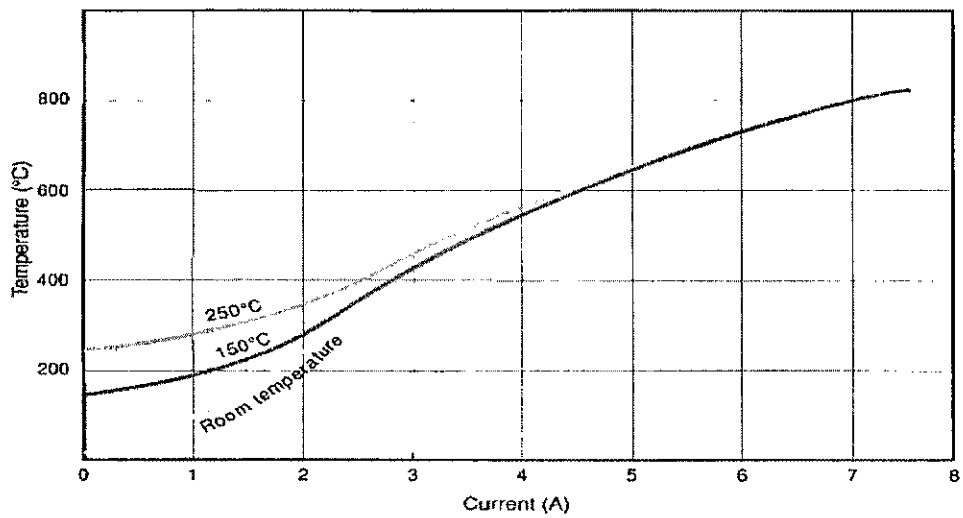

Figure 24: Temperature versus current for SAEs AMD sources [23].

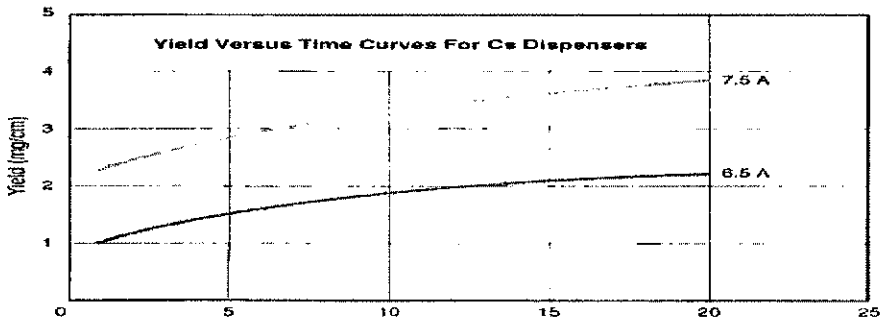

(a)

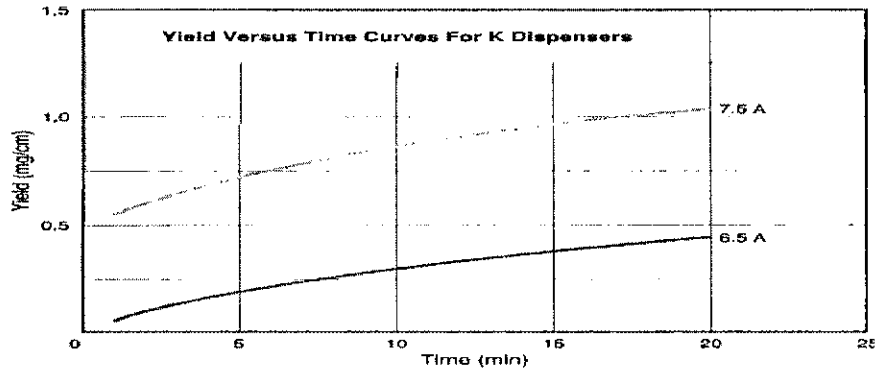

(b)

Figure 25: Yield versus time for 6.5 and 7.5A operational currents: (a) Cs and (b) K [23].

As aforementioned, the experimental trials utilized a second alternative source for cesium deposition. The second source, and hence new setup, was pursued after the initial use of the SAEs cesium sources did not produce the desired result. The second setup, utilized an effusion cesium source, shown in Figure 27. In a Cs effusion source, the cesium is placed in bottom of the j-tube, i.e. the reservoir. Hence, the cesium ampoule is emptied into the tube prior to a bake and the region above the second pinch off is removed once the cesium settles

to the bottom. A resistive heater is wound around the hot gas inlet, and all parts behind the flange are insulated in fiberglass and bake tape. When a heater reaches a high temperature of ~500C, the heat is conducted to the reservoir and the cesium is vaporized into the delivery tube and finally out into the chamber. A second effusion source will be assembled in the future to vaporize K to the substrate.

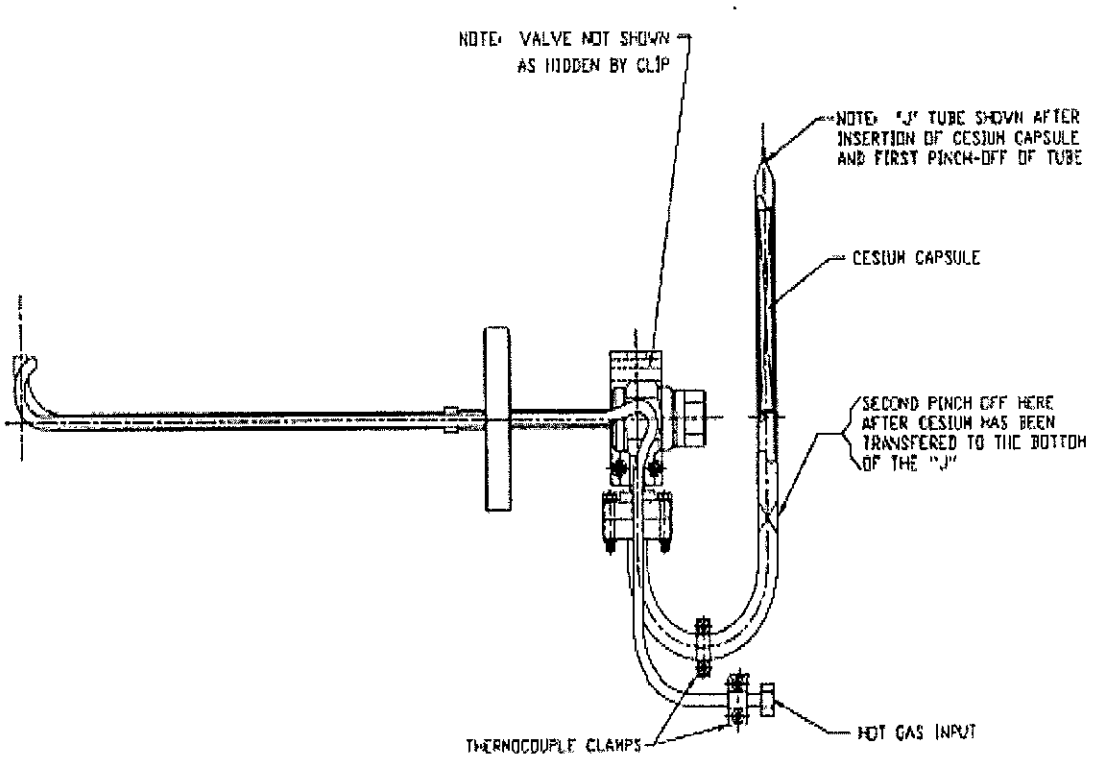

Figure 26: Effusion source schematic [24].

3.3 Vacuum Clean Procedures and Vacuum Establishment

3.3.1 Cleaning Procedures

All parts inserted into the chamber vacuum environment, as well as vacuum surfaces, need to be "clean'. 'Clean' generally means to be free of

contaminants that reduce the quality of a vacuum environment. Therefore, these parts and surfaces require a rigorous cleaning procedure to accomplish this state. The typical cleaning procedure involves placing vacuum parts within an ultrasonic bath containing different solvents: microclean, acetone, methanol and finally water. The parts are then dried with a nitrogen air gun. As a precaution, all vacuum parts are only worked on in a cleanroom and are held with vinyl gloves to avoid contamination by skin tissue or oils. When working with acetone, special acetone-resilient gloves are worn as opposed to vinyl gloves that are dissolved by acetone. Moreover, all parts are placed on lint-free paper or wipes when being worked on, and only wiped using this material. Furthermore all cleaned parts kept in storage are placed within a sealed plastic bag to protect them from all ambient contaminants. Alternatively, vacuum parts can also be wrapped in lint-free paper and a second layer of aluminum foil wrapped around the lint-free paper as a final shield against dust and other particles.

3.3.2 Vacuum Establishment and Baking

As aforementioned, the film growth for experiment trials were conducted in a vacuum chamber under very high vacuum pressure typically 10^{-7} Torr. To obtain this vacuum level involves a two-stage process. The first stage is carried out without the aid of an ion pump because a vacuum level corresponding to 3mA or below, in terms of ion pump current, is necessary before an ion pump can remain on to maintain a vacuum environment without being damaged in the process. Therefore for the first stage, the ion pump is off, and a roughing pump is connected to the chamber via a chamber side-arm and valve assembly. The pump

is used to 'pump down' the chamber, i.e., to remove air from the chamber and establish an initial but relatively poor vacuum. The pump down is continued until the ion pump can 'turn on', that is, begin operation at 3mA or below. Typically an ion pump can turn on at 10mA, as long as the chamber has no leaks. The pump-down will steadily continue to drop the chamber pressure to below 3mA. This pump down process can be aided by activating non-evaporating getters (NEGs). NEGs are essentially convoluted metal plates that absorb vacuum contaminants such as water on these metal surfaces. By running current through these plates, that is 'activating them', the water molecules can be vaporized and hence further water can be removed from the vacuum cavity. At this point the chamber is ready for the 'bake' process.

A 'bake' refers to the thermal heating of the internal cavity of a vacuum chamber, with the purpose of vaporizing higher-boiling-point substances for easy removal by the ion pump. This process typically involves enclosing the chamber within stainless steel panels forming a box around the chamber. One of the panels has a heater and air blower attached to it to vent hot air into the box cavity. The heat from the air is then conducted by the chamber walls to heat the inner surfaces. The temperature within the heating box is monitored using thermocouples that are in contact with the chamber surface. One thermocouple "readout" is connected to the bake controller to in order to appropriately increase or decrease the heater temperature as the heating cycle is completed. The heating cycle typically begins with a ramp up from room temperature (20 to 25C) up to the temperature high point where it remains for a significant number of hours

before ramping back down to room temperature. In the experiments of this work, the maximum temperature was kept to 160C due to the tolerance of the thickness monitor's BNC temperature sensitive connection outside the chamber. The standard heating cycle utilized in the research work is displayed in Figure 28. The graph shows a ramp up from room temperature (20C) to a temperature of 160C where this temperature is maintained over a 30 hour period. Over the 30 hour period, most of the water in the chamber is vaporized and removed from the chamber by the ion pump. Therefore, over this period of time, the ion pump current undergoes an increase to a peak value that is maintained over the time it takes to remove this water. This is followed by a steady decline in the ion pump current as the water pressure in the chamber decreases. A typically bake curve for a standard bake in the experiment is displayed in Figure 29. The plot shows the variation of ion pump current I_p for the change in temperature based on the temperature cycle.

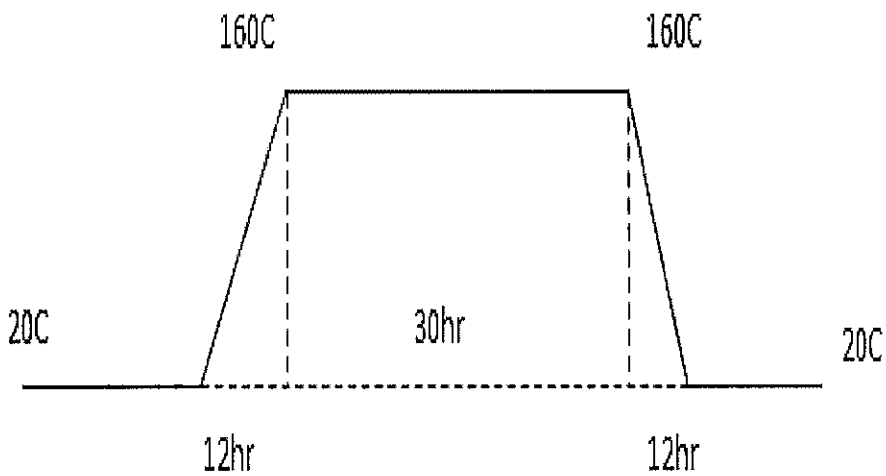

Figure 27: Standard bake ramp cycle.

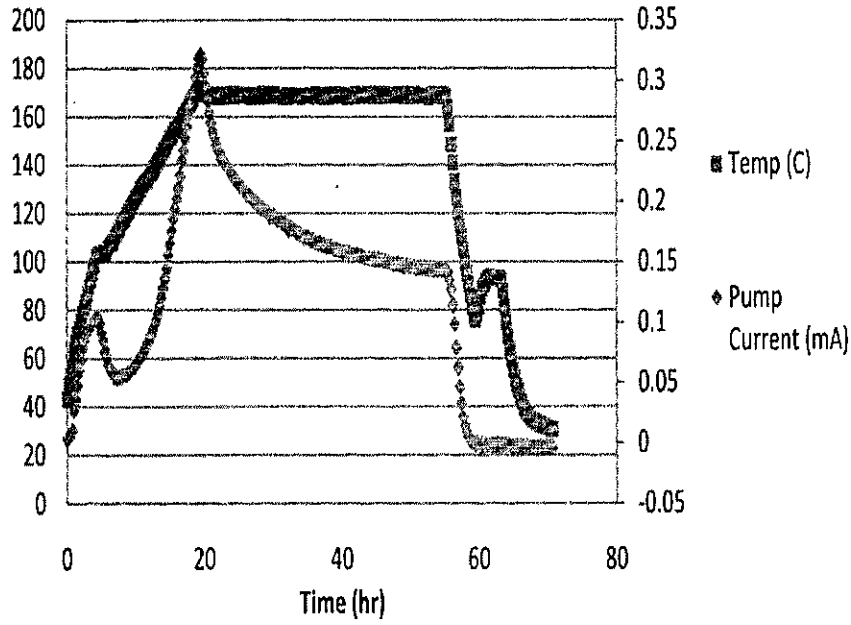

Figure 28: Temperature and current data for actual bake ramp cycle.

3.4 Data Recording

Data recording for the experiments primarily utilized virtual instruments (VIs) that were fed data via a General Purpose Interface Bus (GPIB) of Data Acquisition (DAQ) hardware. The data collected included bake data, which utilized the "Bake Recorder.VI" instrument. On the other hand, the collection of photocurrent data, and hence quantum efficiency data, utilized the "Picoammeter.VI" instrument. The Graphical User Interfaces (GUI)s and corresponding block diagrams for the Bake Recorder VI and Picoammeter VI are shown in Figure 30 (a) and (b), and Figure 31 (a) and (b), respectively.

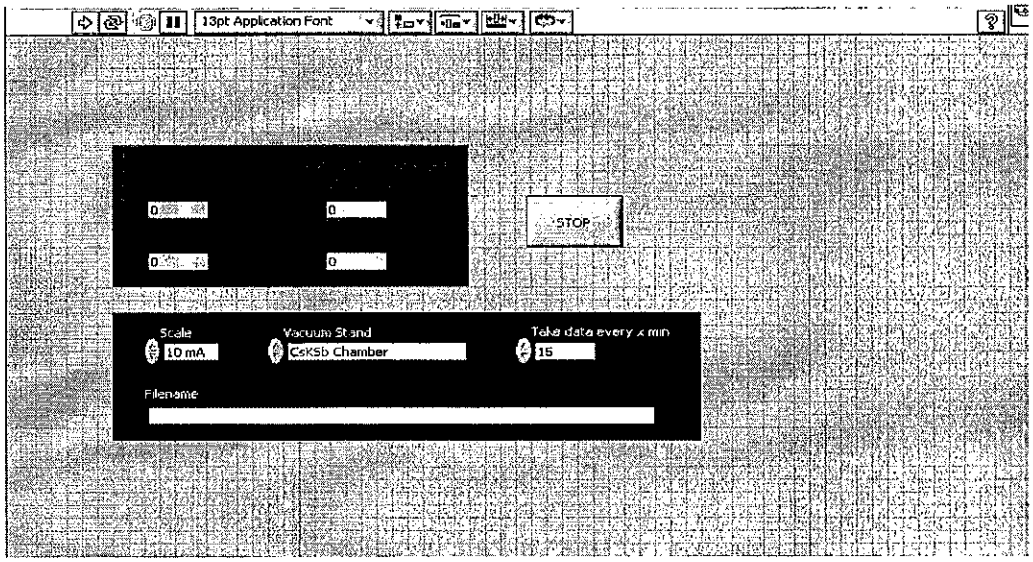

(a)

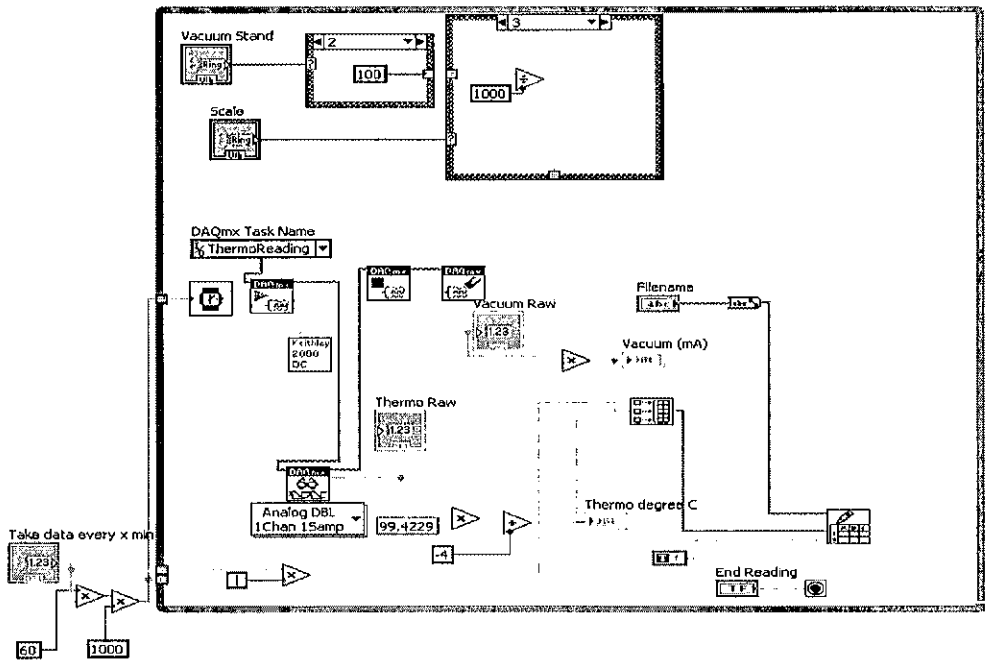

(b)

Figure 29: Bake Recorder VI (a) GUI and (b) Block Diagram.

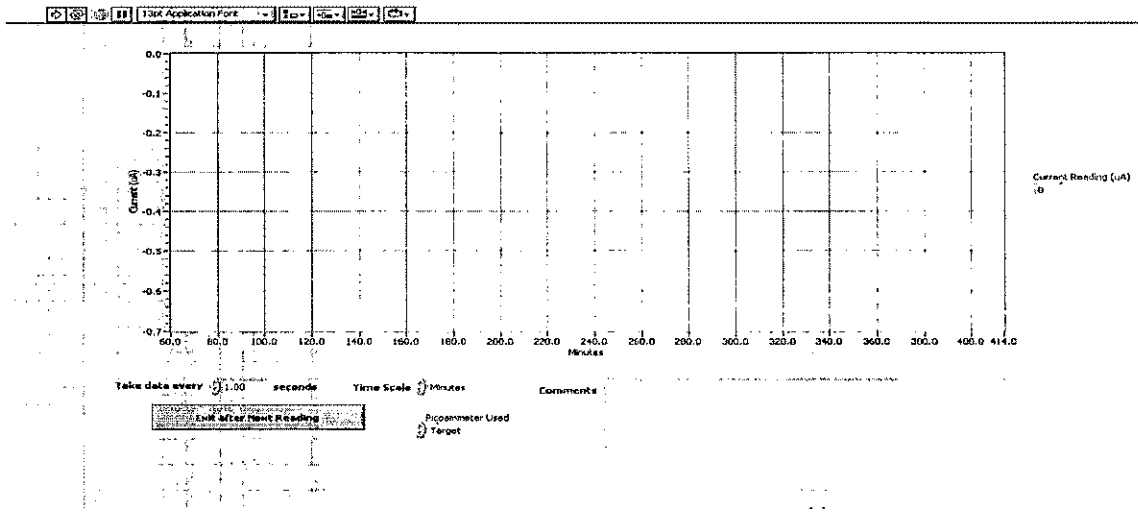

(a)

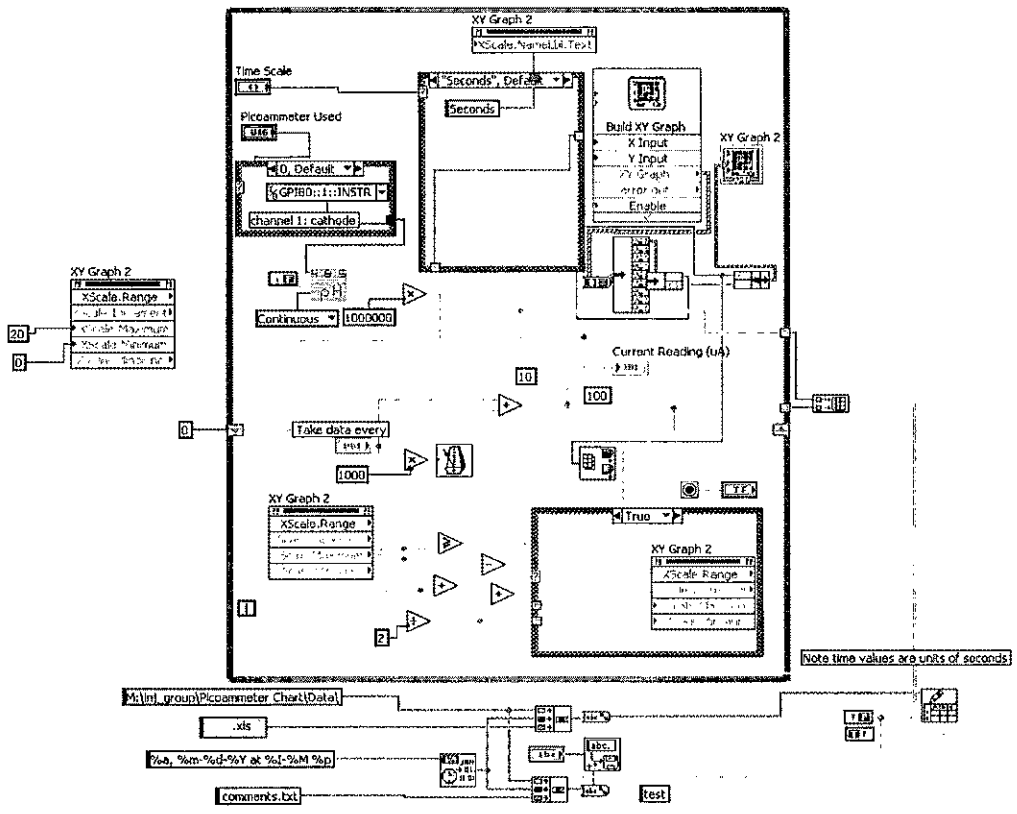

(b)

Figure 30: Picoammeter VI (a) GUI and (b) Block Diagram.

The primary functioning of the Bake Recorder VI is as follows: a numeric input via the GUI sets the time interval for data collection. This interval time sets a periodic delay in the execution of the program loop. The input data are received from two sources, namely a thermocouple reading of the chamber temperature and the ammeter reading of the ion pump current. The raw chamber temperature data are read via DAQ hardware, this temperature is then converted to degrees Celsius scale, as seen in the block diagram. The scaled vacuum pump current data are also read. These two data sets as well as the time data are coupled into an array and written to a specified file. The picoammeter VI works by collecting data at a specified time interval. In this case the current data are read via a GPIB interface. The anode current from the chamber is fed into the analog channel which is linked to the GPIB. The VI displays an XY graph on the GUI representing the Photocurrent vs Time data. The GUI allows for the change of scale of the graph axis and the appropriate rescaling is implemented and displayed in the GUI plot. The recorded current is displayed as a 'double'-valued number in the GUI in microamperes. This current data for the incremental time intervals are then collected into a two-dimensional array and written to a spreadsheet, located in a user-specified folder.

3.5 Experiment Methodology

3.5.1 Sequential Depositions

The experimental trial methodology utilized a sequential deposition approach similar to that of Dowell [17], a similar approach is also used by

BrookHaven National Laboratory (BNL). The sequence of element deposition from their respective sources started with antimony, then potassium and finally cesium. Therefore, every experimental trial began with the deposition of an antimony layer. The recording of current data, i.e. photocurrent and hence QE data, would also be initialized upon the onset of cesium deposition. The crystal thickness monitor was utilized to monitor the respective thicknesses of deposited antimony, and potassium. In regard to cesium, the thickness is regarded as QE dependent; therefore the deposition of cesium would be continued until a maximum QE was obtained.

The deposition of antimony starts with a pre-heating of the antimony resistive filament, the filament contains a crucible with antimony pellets in it. The pre-heat is 5 minutes in length at a current of ~20A. Following the pre-heating, the current is increased to ~23A, and the thickness monitor gauge is observed as the antimony thickness reaches a desired value. The source is turned off prior to obtaining the exact desired thickness because additional time is required for the deposition rate from the source to return to a zero value. During this period there is an approximately exponential decay in a rate that results in the deposition of further material. The next material to be deposited, with respect to fabricating K_2CsSb, is potassium. The potassium source is vaporized from a SAEs source. The thickness monitor gauge was utilized to estimate the grown thickness of potassium, approximately twice the thickness of the antimony layer is deposited on to the substrate. In the fabrication of Cs_3Sb, the potassium deposition stage is bypassed, and cesium deposition immediately follows. The cesium effusion

source required that the effusion heater, tube and reservoir be at specific temperatures before, the valve linking the cesium reservoir and the delivery tube could be opened. The heater of the effusion tube was heated using a 240V variac; with a 78% voltage setting. Once the heater reaches a temperature of ~500C, the delivery tube is simultaneously heated via conduction to ~231C, and the reservoir to ~192C. When these temperatures are reached the valve may be opened, allowing cesium vapor from the reservoir to channel into the delivery tube, eventually reaching the tube opening and escaping into the chamber.

With respect to the experimental parameters of substrate temperature, antimony thickness, anode voltage bias, and substrate material, the following setup was chosen. The temperature of the substrate was maintained at 150C throughout the deposition of the three elements. The substrate material was molybdenum brazed to the end of a stainless steel stalk. The illumination of the substrate on the onset of cesium deposition was carried out using a 532nm and 4.28mW green Continuous Wave diode laser. Hence, electromagnetic radiation within the visible spectrum was utilized as the photon energy source. Antimony thickness variation experiments involved depositing a required thickness of Sb followed by the deposition of cesium until a maximum QE was obtained. Then the fabricated crystal would undergo a 'blowoff'; where the substrate temperature was stepped up to 550C to vaporize any compounds on the substrate, before re-depositing a new Sb thickness. Temperature variation was not conducted for the growth of the Cs3Sb film. However, a temperature drop from fabrication temperature (150C) to room temperature of ~20C was observed. Variation of laser

power was implemented using varying power transmission slides placed in the path of the laser beam prior to it reaching the substrate surface.

CHAPTER IV

RESULTS AND DISCUSSION

4.1 Introduction

The following sections present the data collected from experimental trials towards producing a cesium potassium antimonide thin film to be used as a photocathode. However, the preliminary experiment was aimed at producing a cesium antimonide thin film. Generally the successful growth of a cesium antimonide binary compound is a significant milestone in developing feasible alkali antimonide stoichiometric crystals. Each sub-section of this chapter addresses a specific property variation and discusses what would be expected in each case, the relative significance in comparison to cesium potassium antimonide and the conclusions that can be drawn in each case are also discussed. The work done after the successful Cs_3Sb film growth was aimed at investigating properties of a binary antimonide. Specifically, a typical QE versus Time curve during the last phase of a film growth is presented in Sectin 4.1.

An important property that corroborates the presence of a photocathode is the change in quantum efficiency with laser power variation. The effect of varying the antimony thickness and the resultant QE is researched. Furthermore, temperature variation during the following and during deposition is also investigated in Section 4.3. The photoemissive lifetime of the grown film was also investigated under two conditions; one data set observes the photocathode lifetime under illumination conditions over 18 hour time period. The second data set

investigates the dark lifetime of the grown film, where the photocathode experiences no illumination over a given period of time and we observe the drop in QE when no electromagnetic radiation influences the film can be observed. These data are required to understand the films resilience over time when not under operation.

4. 2 Cs_3Sb Film Growth

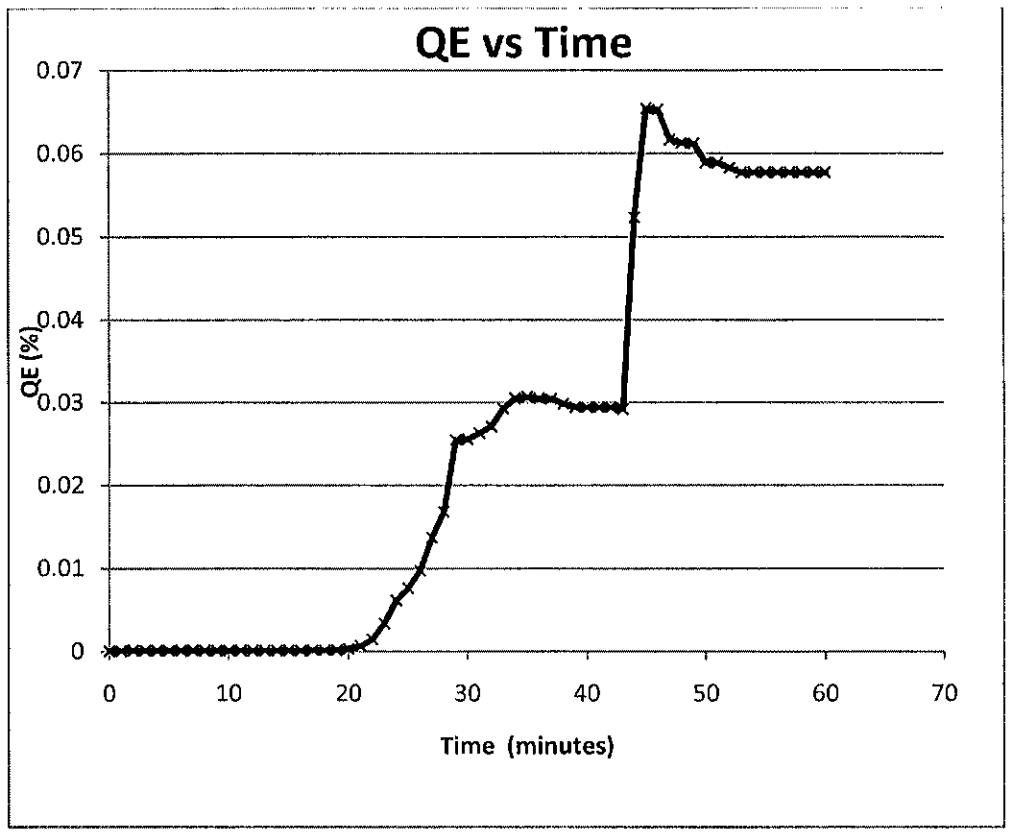

Figure 31: QE versus Time for a Cs_3Sb thin film.

Figure 31 shows the successful growth of a Cs_3Sb thin film. The data are obtained from time t =0; on the onset of cesium deposition and continued until an appreciable QE value is obtained. The cesium deposition is halted once a rollover

in the QE is observed at approximately 35 minutes. The sharp increase in QE at ~47 minutes is an artifact of the experimental apparatus, and corresponds to when the effusion cesiator was pulled away from the substrate, thereby altering the electrostatic collection efficiency of the anode. From the curve above, QE rolls over. The final QE from this was 0.065%, which about a factor of 100 lower than the desired goal, but represents one of the early successes in making an alkali-antimony photocathode.

4.3 QE and Laser Power Variation

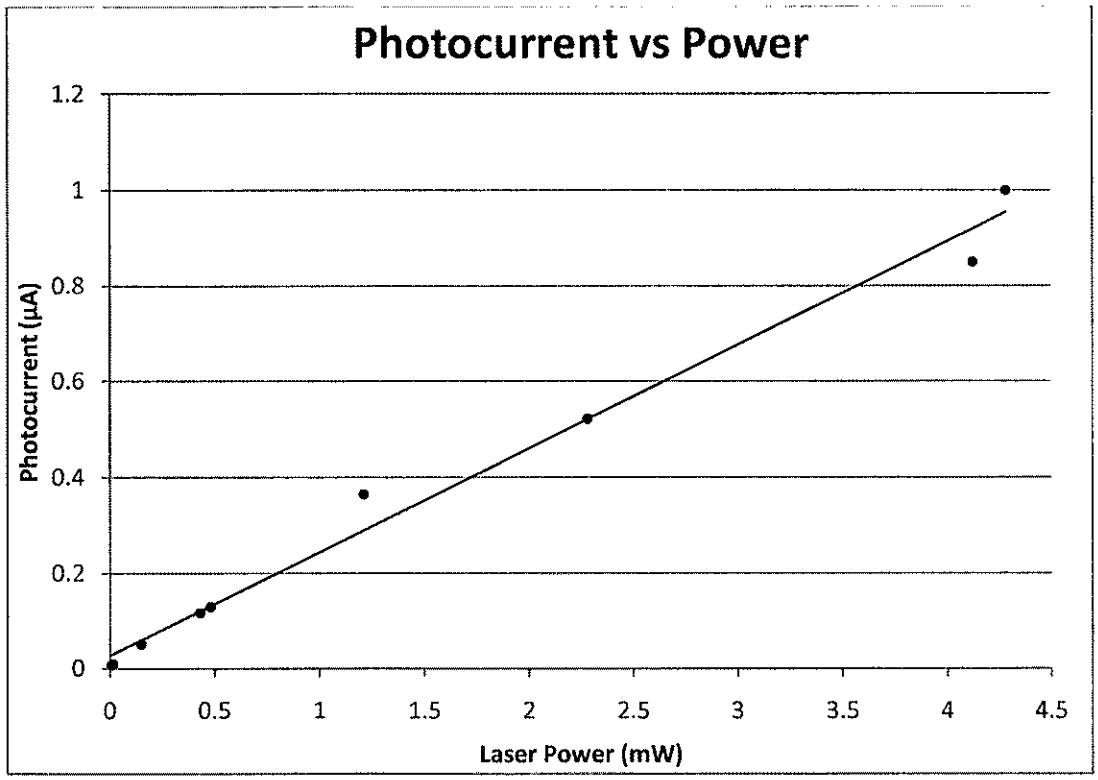

(a)

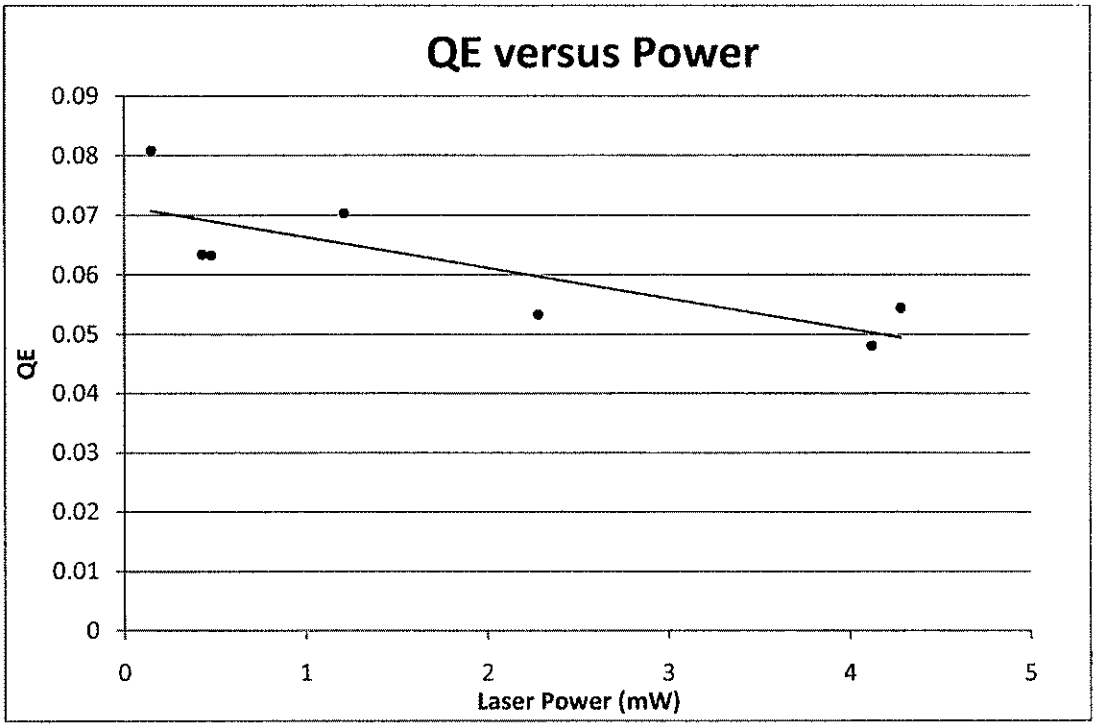

(b)

Figure 32: (a) Photocurrent versus time for a Cs_3Sb thin film (b) QE versus power.

Figure 33a and 33b, shows how varying the laser power affects the Quantum Efficiency. Although it is intuitively understood that a drop in laser power will cause a directly proportional (and approximately linear) drop in the QE of the film, it is necessary to collect these data to confirm expected results. Generally, power is related to energy in the following way corresponding to equation $p = {}^{dw}/_{dt}$. In this equation, p is the power, which is equated to a change in the elemental optical energy quantities over an elemental change of time. Hence, the reduction in energy, i.e. reduction photons delivered to the crystal causes a drop in the quantity of electron elevated to emissive energy levels. The best-fit

line plotted for the data in Figure 33a estimates ~ 0.2μA current increase for every milliWatt of increased laser power.

4.4 QE versus Anode Bias

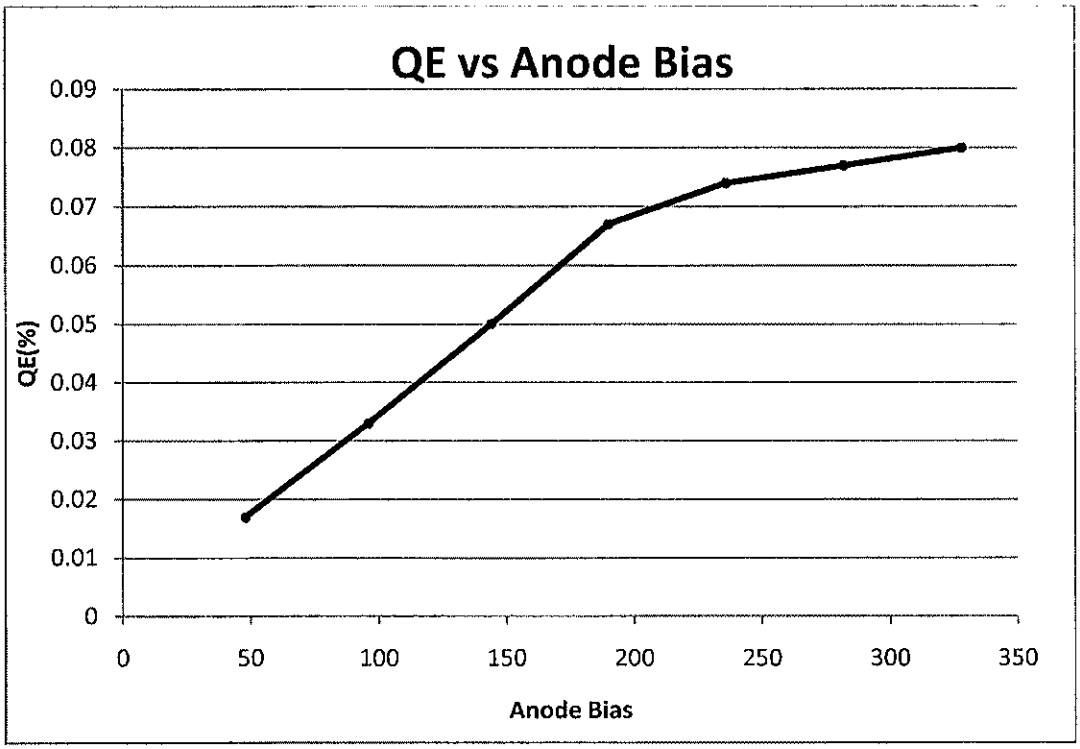

Figure 33: QE versus anode Bias.

The QE versus Anode Bias plot of Figure 33 demonstrates the effect of increased electric field on the obtained photocurrent. Theoretically, it is known that metals typically display very low QE in comparison to alkali antimonides even under high electric fields. Most metals have QE around ~0.01%. By increasing the bias clear evidence is obtained that the grown film exceeds metallic photoemissive limits. This provides additional proof of grown Cs_3Sb since physical stoichiometric confirmation could not be obtained by means of x-ray spectroscopy or other methods.

4.5 Quantum Efficiency Variation for Antimony Deposition Thickness

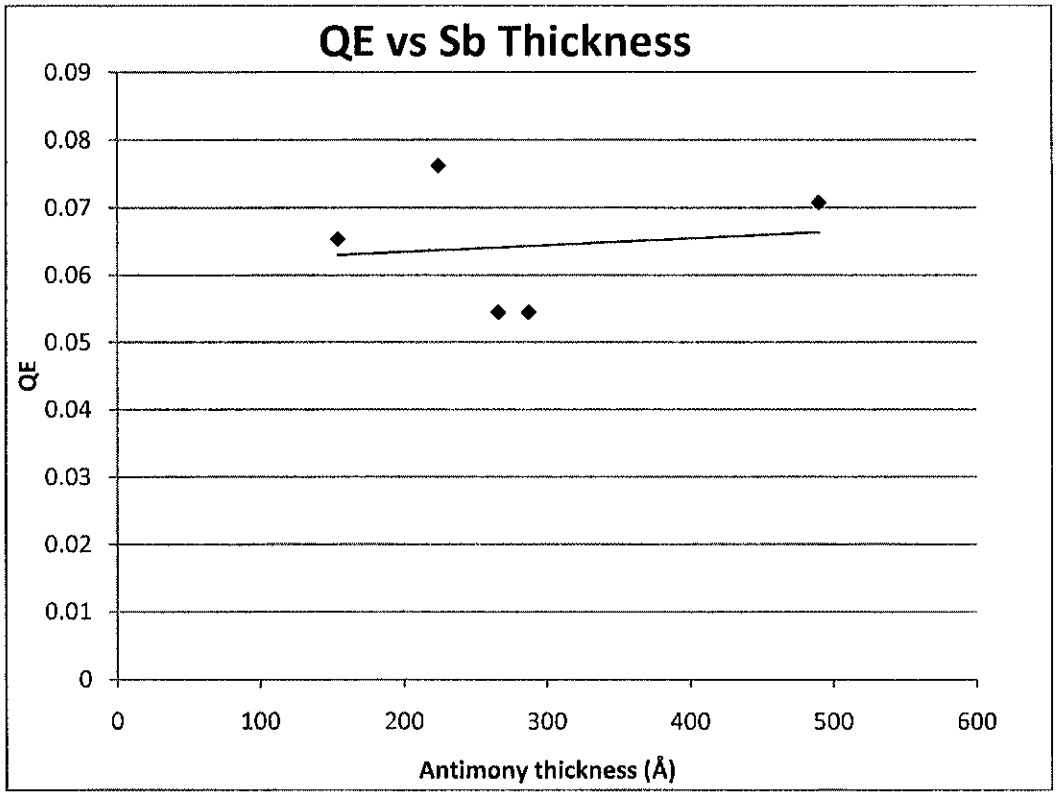

Figure 34: QE versus antimony thickness.

The above data of Figure 34 investigate the influence of the thickness of the antimony layer on the QE from a Cs_3Sb thin film. Seven thicknesses data points and the corresponding QE is plotted in the curve above. The thicknesses listed are based on the estimated substrate thickness derived from the AFM characterization of the antimony source deposition rate. An approximate substrate to monitor reading of 6:1 was obtained. Depositing antimony thicknesses greater than ~420Å failed to produce a QE rollover within an hour of cesiating. A reasonable explanation is that the greater antimony thickness requires a greater mass of cesium to diffuse into the antimony bulk and form the appropriate

stoichiometry. The above results show that the thickness of the antimony layer between 180Å and 420Å generally does not have a significant impact on the QE.

4.6 Photocurrent versus Temperature

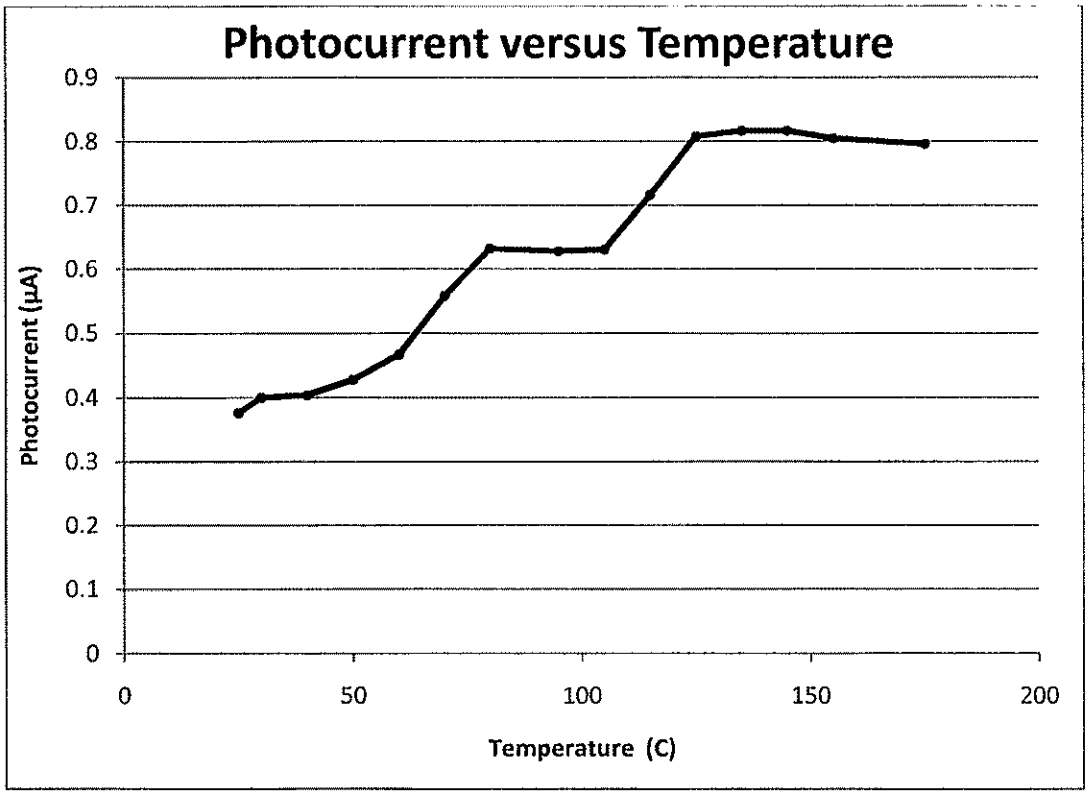

Figure 35: Post-deposition photocurrent versus temperature drop.

Figure 36 shows a curve of the photocurrent versus a natural temperature drop of the substrate temperature. Ideally the grown crystal should approximately maintain its QE and photocurrent values as the substrate temperature is reduced. The data show a significant drop in photocurrent as the temperature is dropped. This could possibly be attributed to cesium migration occurrence since the cathode is allowed to cool at a natural rate. Expedited cooling utilizing nitrogen

airflow may allow the stoichiometry to remain unchanged in terms of cesium composition and hence, produce a cooled cathode while maintaining peak QE.

4.7 Lifetime of Cs_3Sb film

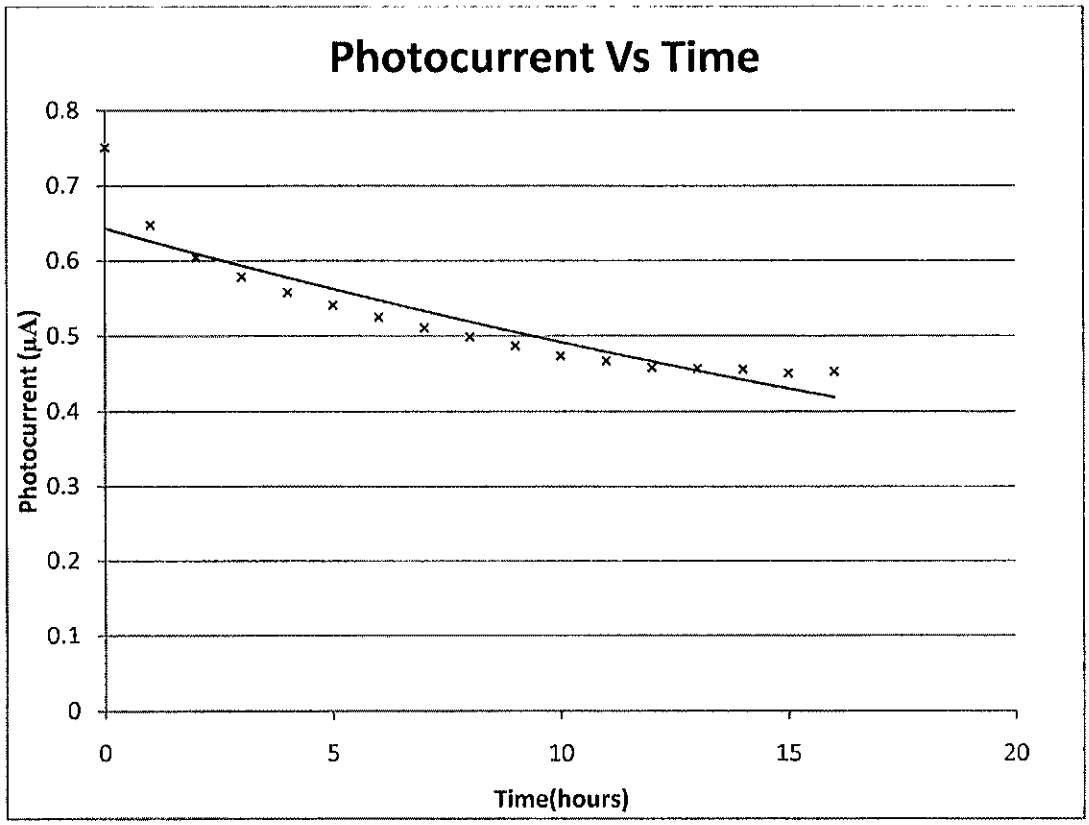

Figure 36: Cesium antimonide curve of photocurrent versus time.

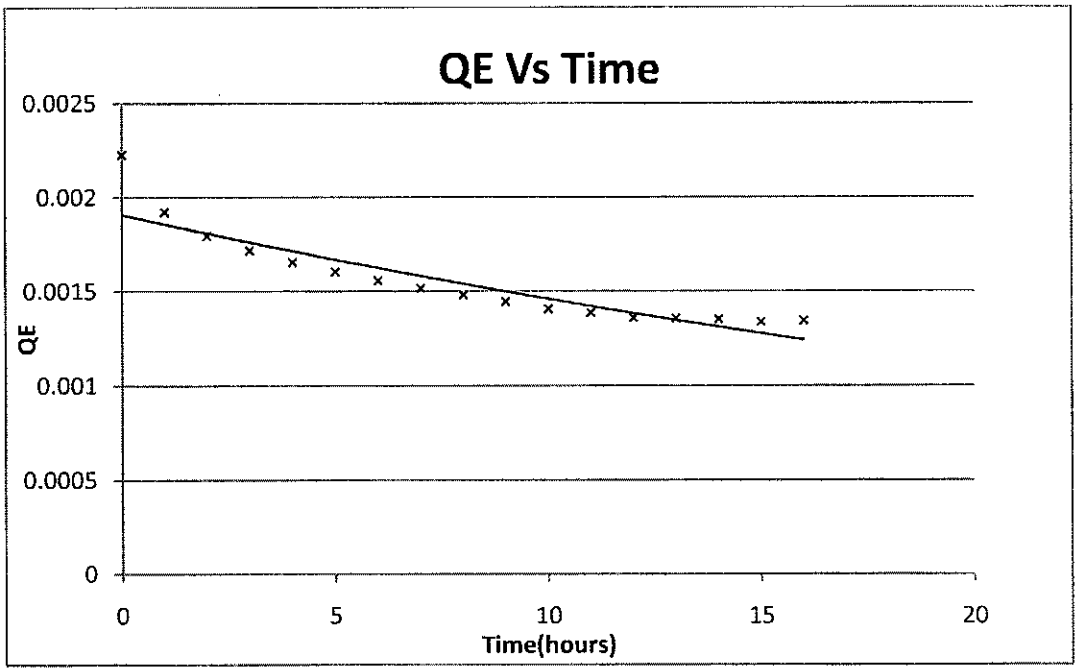

Figure 37: Cs_3Sb curve of QE versus time.

The data above give the lifetime measurement under the illumination of a 532nm, 4.28mW green laser. The following QE decay rate and QE relation at an instant in time, t can be used in this context.

$$-\frac{dQ(t)}{dt} = cQ(t), \tag{13}$$

The constant of proportionality c, is called the decay constant. The mean lifetime is, by definition, the reciprocal of the decay constant. Therefore lifetime $T_{lifetime} = 1/c$. The best-fit exponential approximation of the above plot, approximates a decay constant of 0.027 and the lifetime found by finding the corresponding decay constant's reciprocal. Hence, the lifetime for this cathode is approximately 37 hours. This is a favorable result since lifetime of illuminated GaAs cathodes can be significantly shorter.

CHAPTER 5

CONCLUSIONS AND SCOPE FOR FUTURE WORK

5.1 Thesis Summary

The successful attainment of measurable quantum efficiency for the grown cesium antimonide cathode validates the growth technique and functionality of the deposition system. Therefore, a sufficient quality vacuum environment for film growth has been established. Moreover, adequate thermal sources that dispense material in a reliable manner that create reproducible results can be obtained from this fabrication technique. There are slight variations in QE depending on the site of incident radiation. The incident laser spot on the photocathode is traversed through five sites and stationed at the highest QE yielding location. The experimental results confirm several positive attributes for alkali antimonide thin films used as photocathodes, and as are discussed in the following paragraph.

The following conclusions can be drawn from the variation of antimony thickness and the effect on quantum efficiency. The mean photocurrent obtained from five grown photocathodes was 1.14μA, with a standard deviation of 0.16 μA. This indicates that there is no significant change in QE when the antimony thickness is varied between approximately 100 and 400 angstroms. Furthermore, it is safe to conclude that by growing the antimony layer to thicknesses greater than 400 angstroms simply extends the cesiation time to achieve maximum QE, but does not increase it significantly. Once a cathode is fabricated, the substrate

temperature is 150C. By monitoring the temperature versus QE for a drop from 150C to room temperature, it is shown that the temperature drop does have a significant effect on the QE.

Theoretically a linear increase of photcurrent with incident laser power is expected and this property is verified in the QE versus Power data. Furthermore the QE obtained of alkali antimonides is expected to be higher than those of metals in general. This aspect is also supported since the increase in applied electric fields, presented in the QE versus applied anode voltage data, shows increasing values of the Quantum efficiency exceeding those obtained from metals.

The cesium antimonide cathode is a significant achievement that helps demonstrate the potential of alkali antimonides. The future of the research is to successfully fabricate multialkali antimonides with attractive photocurrent properties. Specifically, the cesium potassium antimonide photocathode will be attempted. The end goal will be to produce a cathode that produces greater QE than currently achieved using GaAs. At Jefferson Laboratory these values correspond to a QE in the 5% to 20% range at 532nm, with 500C of charge extracted before the QE falls to 1/e of its initial value. Therefore, it is hoped that a CsK2Sb photocathode can provide many more coulombs before QE falls by the same amount, and produce QE that is greater than 5% at 532 nm.

5.2 Future Work

The successful growth of cesium antimonide is a preliminary achievement in the long-term goal of producing a mulitalkali antimonide photocathode at Jefferson Laboratory. Specifically the research will be extended to grow a cesium potassium antimonide photocathode. The cesium antimonide photocathode produced a 0.07% quantum efficiency value. This is a relatively low QE value. Therefore, further experiments will have to be performed to optimize this value. The following parameters will have to be explored to achieve higher QE values from Cs_3Sb: The substrate material, temperature of the substrate during antimony and cesium deposition, wavelength variation and multiple depositions. However, this next phase of experiments will be continued by the staff of scientists at the Source Lab of Jefferson Laboratory. The following steps will be required before an attempt at growing cesium potassium antimonide can be made: The installation of a secondary effusion source, in this case the effusion j-tube will be loaded with a potassium ampoule to fill the tube with potassium. Therefore, the effusion source will dispense potassium vapor upon reaching operational temperature. Once the secondary source is installed, a deposition methodology similar to that used for the Cs_3Sb photocathode, will be utilized to grow the K_2CsSb film. Once a K_2CsSb film is grown, there will be similar data collected regarding, potassium thickness variations, temperature variations during deposition, wavelength variation in order to optimize the QE. Once a successful K_2CsSb photocathode is grown, the most critical test will be to extract beam from the cathode in identical conditions as those currently applied to GaAs in an accelerator. Under these

conditions, if the QE of K_2CsSb exceeds a 5% range and a charge of 500C can be extracted from the film before a 1/e drop in its QE, then the research would be a success. In particular, Jefferson Laboratory would have a K_2CsSb photocathode that can be utilized for light source applications.

APPENDICES

Appendix A: Used Symbols

Symbol	Quantity	Unit
Å	angstrom	10^{-10}meters
I_p	photocurrent	Amperes
v	frequency	Hertz (Hz)
m	mass	kg
l	length	Meter (m)
π	Pi (constant)	3.14159…
P_{opt}	optical power	Watts
k	wavevector	1/m
Nq	frequency constant	Hz
c	speed of light	$3x10^8$m/s
Pq	density of quartz	$2.65g/cm^3$
G	shear modulus	dynes $/cm^2$
C	transverse (shear) wave velocity	cm/s
fq	resonant frequency of uncoated quartz crystal	Hz
ρ	density of material	g/ cm^3
TK	thickness of deposited material	Å
dcry	distance from the source to the crystal	m
dsub	distance from the source to the substrate	m

Appendix B: Prefixes

Symbol	Abbreviation
Giga	10^{9}
Mega	10^{6}
Kilo	10^{3}
Deci	10^{-1}
Centi	10^{-2}
Milli	10^{-3}
Micro	10^{-6}
Nano	10^{-9}
Pico	10^{-12}
Femto	10^{-15}
Atto	10^{-18}

Appendix C: Procedures for Making Cs_3Sb Cathodes

The cathode growth technique utilized a sequential deposition approach similar to that of Dowell [17], however, the temperature, substrate material and other deposition parameters are unique to the chamber.

1. Preheat the cesiator effusion source: A 240V variac can be used to power the effusion heater. The variac setting must be at 78%. Connect a nitrogen line to the nitrogen gas inlet, and flow nitrogen at 15SCFH (standard cubic feet per hour). Allow the effusion delivery tube temperature to reach ~220C before utilizing the cesium source.
2. Confirm the chamber electrical biasing is as follows: The cathode is "floated" and therefore has no bias applied to it, however the anode ring is connected to a ~+240V bias.
3. Power the stalk heater to achieve a substrate temperature of ~150C. Stalk heater to substrate temperature conversions may have to be applied. Typically the substrate temperature obeys a linear relationship to the stalk heater temperature: ~80% of the stalk temperature.
4. Ensure the cesium and potassium sources are retracted so they are not below the substrate. Furthermore, ensure the thickness monitor controller parameters are set for the deposition of the appropriate material (initially antimony).
5. With the thickness monitor controller parameters set for antimony, the deposition of an antimony layer can begin. To pre-heat the antimony boat, run a current of ~20A through the Sb source filament. Following the pre-

heating, increase the current to ~23A or lower, and observe the displayed thickness on the monitor gauge. Note the deposition rate as the thickness approaches the desired value, ~25-65 angstroms, and account for additional deposited material as the rate exponentially drops to zero.

6. The substrate material was molybdenum fused to the end of a stainless steel stalk. The illumination of the substrate on the onset of cesium deposition is carried out using a 532nm and 4.28mW green CW laser, hence electromagnetic radiation within the visible spectrum is utilized as the photon energy source.

7. Retract the antimony source before inserting the cesium source. Ensure the delivery tube heater and reservoir are at required temperatures before its valve can be opened. The heater should be at ~500C, the delivery tube ~231C, and the reservoir ~192C. The valve can now be opened. Start data recording for the photocurrent emitted, the cesium thickness is not monitored but deposition is continued to obtain the optimum QE. Then retract the cesium source and close the effusion source valve.

REFERENCES

[1] J. J. Thomson, "On bodies smaller than atoms," *The Popular Science Monthly,* pp. 323–335, Aug. 1901.

[2] C. Hernandez-Garcia, P. G. O'Shea, M. L. Stutzman, "Electron Sources for Accelerators," *Phys. Today*, pp 44-48, Feb. 2008.

[3] J. Kessler, *Polarized Electrons*, 2nd ed. Berlin: Springer, 1985.

[4] D. M. Mattox, *Handbook of Physical Vapor Deposition (PVD) Processing Film Formation, Adhesion, surface Preparation and Contamination Control*, Park Ridge, NJ: Noyes Publications 1998.

[5] E. R. Cohen, T. Cvitas, J. G. Frey, B. Holmstrom,K. Kuchitsu, *Quantities, Units and Symbols in Physical Chemistry*, 2nd ed., Oxford: Blackwell Science, 2007.

[6] J. E. Mahan, *Physical Vapor Deposition of Thin Films*, New York, NJ: Wiley, 2000.

[7] V.K. Zworykin, E. G. Ramberg, *Photo-electricity*, New York: Wiley and Sons, 1949.

[8] A.R. Ettema, R.A. de Groot, "Electronic structure of Cs_2KSb and K_2CsSb," *Physical Review B*, Vol. 66, Jan. 2002.

[9] C. Ghosh, B. P. Varma, "Preparation and study of the properties of a few alkali antimonide photocathodes," *Journal of Applied Physics*, Vol. 49, No. 8, pp. 4549-4550, Aug. 1978.

[10] L. Galan, C. W. Bates Jr., "Structure of multialkali antimonide photocathodes studied by X-ray photoelectron spectroscopy," 1981 Journal of Physics D: Applied Physics, Vol. 14, pp. 293 -298.

[11] John Smedley, private communication, Jun. 2010.

[12] R.W. Wood, "Remarkable Optical Properties of the Alkali Metals", *Physical Review*, Vol. 44, pp. 353-359, June, 1933.

[13] P. Michelato, P. Gallina, C. Pagani, "Alkali photocathode development for Superconducting rf guns", *Nuclear Instruments and Methods in Physics Research*, Vol. A 340, pp. 176-181, 1994.

[14] R. L. Ternes, S. Z. Bethel, D. G. Janky, "A statistically-designed experiment for assessing cesium-potassium – antimonide photocathode fabrication parameters," *Nuclear Instruments and Methods in Physics Research*, Vol. A 318, pp. 401-409, 1992.

[15] S. Moss. (2005), *NSF awards Cornell $18 million to develop a new source of X-rays* [Online]. Available: http://www.news.cornell.edu/Chronicle/05/2.24.05/ERL.html [Accessed Aug.,2010]

[16] J. Smedley, T. Rao, E. Wang, "K_2CsSb Cathode Development", American Institute of Physics Conference Proceedings, Vol.1149, pp. 1062-1066, Aug. 4, 2009.

[17] D. H. Dowell, S. Z. Bethel, K. D. Friddell, *Nuclear Instruments and Methods in Physics Research*, Vol. A 356, No. 167, 1995.

[18] S.M. Sze, *Semiconductor Devices, Physics and Technology*, 2nd ed., New York: Wiley, 2002.

[19] H. J. Drouhin, C. Hermann and G, Lampel, "Photoemission from activated Gallium Arsenide. I Very-high-resolution energy distribution curves," *Physical Review B*, Vol. 31, No. 6, Mar., 1985.

[20] B. V. Zeghbroeck. (2007). *Light emission and absorption* [Online]. Available: http://ecee.colorado.edu/~bart/book/book/chapter4/ch4_6.htm [Accessed Sept. 10, 2010].

[21] (2010). *Density and acoustic impedance values* [Online]. Available: http://www.inficonthinfilmdeposition.com/en/densityandacousticvalues.html [Accessed Sept. 20, 2010].

[22] (2010). *Baskets and Heaters* [Online]. Available: http://www.rdmathis.com/storev2/category.asp?cat=Baskets+and+Heaters&offset=10 [Accessed Sept. 18, 2010].

[23] (2010) *Alkali Metal Dispensers* [Online technical brochure]. Available: http://www.saesgetters.com/default.aspx?idpage=470 [Accessed Jul. 15, 2010].

[24] B. Dunham, C.K. Sinclair, "Charging the Cesiator on the Illinois/CEBAF polarized electron source," *NPL Polarized Source Group Technical Note #90-3*, May, 1990.

VITA

George Kojo Annobil was born in Cape Coast, Ghana. He attended Old Dominion University from the Fall of 2004 to Spring 2009 when he obtained his Bachelor of Science degree in electrical engineering. He continued on to his master's through an accelerated masters program at Old Dominion University as well, receiving his Master of Science Degree in electrical engineering in May 2011. He is also a member of the Tau Beta Pi Honor Society.